The Astrophysical Journal, 787:139 (18pp), 2014 June 1 doi:10.1088/0004-637X/787/2/139

THE TYPE IIP SUPERNOVA 2012aw IN M95: HYDRODYNAMICAL MODELING OF THE PHOTOSPHERIC PHASE FROM ACCURATE SPECTROPHOTOMETRIC MONITORING

M. Dall'Ora[1], M. T. Botticella[1], M. L. Pumo[2], L. Zampieri[2], L. Tomasella[2], G. Pignata[3], A. J. Bayless[4], T. A. Pritchard[5], S. Taubenberger[6], R. Kotak[7], C. Inserra[7], M. Della Valle[1,8], E. Cappellaro[2], S. Benetti[2], S. Benitez[6], F. Bufano[3], N. Elias-Rosa[9], M. Fraser[7], J. B. Haislip[10], A. Harutyunyan[11], D. A. Howell[12,13], E. Y. Hsiao[14], T. Iijima[2], E. Kankare[15], P. Kuin[16], J. R. Maund[7,20], A. Morales-Garoffolo[9], N. Morrell[14], U. Munari[2], P. Ochner[2], A. Pastorello[2], F. Patat[17], M. M. Phillips[14], D. Reichart[10], P. W. A. Roming[4,5], A. Siviero[18], S. J. Smartt[7], J. Sollerman[19], F. Taddia[19], S. Valenti[12,13], and D. Wright[7]

[1] INAF, Osservatorio Astronomico di Capodimonte, Napoli, Italy
[2] INAF, Osservatorio Astronomico di Padova, I-35122 Padova, Italy
[3] Departamento de Ciencias Fisicas, Universidad Andres Bello, Avda. Republica 252, Santiago, Chile
[4] Southwest Research Institute, Department of Space Science, 6220 Culebra Road, San Antonio, TX 78238, USA
[5] Department of Astronomy & Astrophysics, Penn State University, 525 Davey Lab, University Park, PA 16802, USA
[6] Max-Planck-Institut für Astrophysik, Karl-Schwarzschild-Str. 1, D-85741 Garching, Germany
[7] Astrophysics Research Centre, School of Mathematics and Physics, Queen's University Belfast, Belfast, BT7 1NN, UK
[8] International Center for Relativistic Astrophysics, Piazzale della Repubblica 2, 65122 Pescara, Italy
[9] Institut de Ciències de l'Espai (CSIC-IEEC) Campus UAB, Torre C5, Za plata, E-08193 Bellaterra, Barcelona, Spain
[10] Department of Physics and Astronomy, University of North Carolina at Chapel Hill, 120 E. Cameron Ave., Chapel Hill, NC 27599, USA
[11] Fundación Galileo Galilei - Telescopio Nazionale Galileo, Rambla José Ana Fernández Pérez 7, E-38712 Breña Baja, TF - Spain
[12] Las Cumbres Observatory Global Telescope Network, 6740 Cortona Dr., Suite 102 Goleta, CA 93117, USA
[13] Department of Physics, University of California, Santa Barbara, Broida Hall, Mail Code 9530, Santa Barbara, CA 93106-9530, USA
[14] Carnegie Observatories, Las Campanas Observatory, Colina El Pino, Casilla 601, Chile
[15] Finnish Centre for Astronomy with ESO (FINCA), University of Turku, Väisäläntie 20, FI-21500 Piikkiö, Finland
[16] University College London, Mullard Space Science Laboratory, Holmbury St. Mary, Dorking, Surrey RH5 6NT, UK
[17] European Organization for Astronomical Research in the Southern Hemisphere (ESO), Karl-Schwarzschild-Str. 2, D-85748, Garching b. Mnchen, Germany
[18] Dipartimento di Fisica e Astronomia Galileo Galilei, Universitá di Padova, vicolo dell'Osservatorio 3, I-35122 Padova, Italy
[19] The Oskar Klein Centre, Department of Astronomy, AlbaNova, SE-106 91 Stockholm, Sweden
Received 2013 August 2; accepted 2014 April 2; published 2014 May 13

ABSTRACT

We present an extensive optical and near-infrared photometric and spectroscopic campaign of the Type IIP supernova SN 2012aw. The data set densely covers the evolution of SN 2012aw shortly after the explosion through the end of the photospheric phase, with two additional photometric observations collected during the nebular phase, to fit the radioactive tail and estimate the ^{56}Ni mass. Also included in our analysis is the previously published *Swift* UV data, therefore providing a complete view of the ultraviolet-optical-infrared evolution of the photospheric phase. On the basis of our data set, we estimate all the relevant physical parameters of SN 2012aw with our radiation-hydrodynamics code: envelope mass $M_{\rm env} \sim 20\,M_{\odot}$, progenitor radius $R \sim 3 \times 10^{13}$ cm ($\sim$430 $R_{\odot}$), explosion energy $E \sim 1.5$ foe, and initial ^{56}Ni mass $\sim$0.06 $M_{\odot}$. These mass and radius values are reasonably well supported by independent evolutionary models of the progenitor, and may suggest a progenitor mass higher than the observational limit of $16.5 \pm 1.5\,M_{\odot}$ of the Type IIP events.

Key words: galaxies: individual (M95) – supernovae: general – supernovae: individual (2012aw)

Online-only material: color figures

1. INTRODUCTION

Type II supernova (SN) events are the product of the collapse of a moderately massive progenitor, with an initial mass between 8 $M_{\odot}$ (e.g., Pumo et al. 2009) and 30 $M_{\odot}$ (e.g., Walmswell & Eldridge 2012). According to the classical classification scheme (see Filippenko 1997 for a review), their spectra show prominent Balmer lines, which means that at the time of the explosion they have still retained their hydrogen-rich envelope. "Plateau" Type II SNe (Type IIP) show a nearly constant luminosity for $\sim$80–120 days (Barbon et al. 1979). The plateau is an optically thick phase, in which the release of the thermal energy deposited by the shock wave on the expanding ejecta is driven by the hydrogen recombination front, which gradually recedes in mass (e.g., Kasen & Woosley 2009, Pumo & Zampieri 2011). When the recombination front reaches the base of the hydrogen envelope, the light curve sharply drops by several magnitudes in $\sim$30 days (e.g., Kasen & Woosley 2009; Olivares et al. 2010). This transition phase is followed by the linear "radioactive tail," powered by the decay of ^{56}Co to ^{56}Fe, which depends on the amount of ^{56}Ni synthesized in the explosion (e.g., Weaver & Woosley 1980). In a few cases, the progenitors have been identified in high-resolution archival images and found to be red supergiants (RSGs) of initial masses between $\sim$8 $M_{\odot}$ and $\sim$17 $M_{\odot}$. Available data show an apparent lack of high-mass progenitors, and this fact has been called the "RSG problem" (Smartt 2009). Walmswell & Eldridge (2012) suggested that the dust produced in the RSG wind could increase the line-of-sight extinction, with the net effect of underestimating the luminosity and, as a consequence, the mass of the progenitor. However, Kochanek et al. (2012) pointed out that all work to date, including that of Walmswell & Eldridge (2012), has incorrectly used interstellar extinction laws rather than a consistent physical treatment of circumstellar extinction, which may lead to an

[20] Royal Society Research Fellow.

overestimate of the effect of extinction. Finally, we note that there is evidence that a minor fraction of Type II SNe results from the explosion of blue supergiant stars, the best example being SN 1987A (Arnett et al. 1989). These SNe show a significant variety in the explosion parameters, but they generally display Type IIP behavior. Smartt et al. (2009) and Pastorello et al. (2012) have suggested that less than 3–5% of all Type II SNe are 1987A-like events.

The interest in Type IIP SNe is twofold. First, observations show that Type IIP SNe are the most common explosions in the nearby universe (e.g., Cappellaro et al. 1999; Li et al. 2011). This means that, given their observed mass range, they can be used to trace the cosmic star formation history up to $z \sim 0.6$ (see Botticella et al. 2012; Dahlen et al. 2012). Second, it has been suggested that they can be used as cosmological distance indicators (see Hamuy & Pinto 2002; Nugent et al. 2006; Poznanski et al. 2009; Olivares et al. 2010).

Despite their frequency and importance, only a fraction of Type IIP SNe has been extensively monitored, photometrically and spectroscopically from the epoch of explosion through the late nebular phase. This type of extensive and extended monitoring is only viable for the closest events (typically closer than 10–15 Mpc), as spectroscopic observations become difficult even with 10m-class telescopes, beyond 300 days. Examples with Type IIP SNe with this sort of coverage are SN 1999em (Elmhamdi et al. 2003), SN 1999gi (Leonard et al. 2002), SN 2004et (Maguire et al. 2010), SN 2005cs (Pastorello et al. 2009), SN 2009md (Fraser et al. 2011), and SN 2012A (Tomasella et al. 2013).

Therefore, the occurrence of a nearby Type IIP SN offers us a unique opportunity to collect very high quality photometric, spectroscopic, and polarimetric data from early stages up to the nebular phase. Through the analysis of pre-explosion images, we also have the possibility to compare the progenitor parameters estimated with hydrodynamical explosion codes with the predictions of evolutionary models.

SN 2012aw was discovered by Fagotti et al. (2012) in the spiral galaxy M95 (NGC 3351), at the coordinates $\alpha_{2000} = 10^{h}43^{m}53\overset{s}{.}76$, $\delta_{2000} = +11°40'17\overset{''}{.}9$ on 2012 March 16.86 UT. The magnitude at the discovery epoch was $R \sim 15$ mag and steeply rising ($R \sim 13$ mag, by J. Skvarc on March 17.90 UT). The latest pre-discovery image was on March 15.86 UT (Poznanski et al. 2012). These data allow us to constrain the explosion epoch to March 16.0 ± 0.8 UT, corresponding to the Julian Day (JD) 2,456,002.5 (Fraser et al. 2012a). In the following, we will refer to this epoch as day 0. The designation SN 2012aw was assigned after an early spectrum taken by Munari et al. (2012) on 2012 March 17.77 UT which showed a very hot continuum without obvious absorption or emission features, and subsequently spectroscopic confirmations independently obtained by Itoh et al. (2012) and by Siviero et al. (2012) which showed a clear H_α P Cygni profile, indicating a velocity of the ejecta of about 15000 km s^{-1} (Siviero et al. 2012).

SN 2012aw was also observed in the X-rays with *Swift* (Immler & Brown 2012) between 2012 March 19.7 and March 22.2 UT at a luminosity $L_X = 9.2 \pm 2.5 \times 10^{38}$ erg s^{-1}, and at the radio frequency of 20.8 GHz on March 24.25 UT (Stockdale et al. 2012) at a flux density of 0.160 ± 0.025 mJy. A subsequent radio observation on March 30.1 UT at the frequency of 21.2 GHz revealed a flux density of 0.315 ± 0.018 mJy (Yadav et al. 2012), thus confirming a radio variability. Finally, spectropolarimetric observations with VLT+FORS2 suggested a significant intrinsic continuum polarization at early phases, a possible signature of a substantial asymmetry in the early ejecta (Leonard et al. 2012).

A candidate progenitor was promptly identified as a RSG in archival *Hubble Space Telescope* data by Elias-Rosa et al. (2012) and by Fraser et al. (2012b). Detailed pre-SN multi-band photometry was carried out on space (HST WFPC2 $F814W$) and ground-based (VLT+ISAAC, NTT+SOFI) archival images by Fraser et al. (2012a). Adopting a solar metallicity, they estimated a luminosity in the range 10^5–$10^{5.6}\,L_\odot$ and an effective temperature between 3300 and 4500 K, and a progenitor radius larger than $500\,R_\odot$. Their comparison with stellar evolutionary tracks pointed toward a progenitor with an initial mass between 14 and $26\,M_\odot$. We note that the uncertainties in the Fraser et al. (2012a) parameters are mostly due to the line-of-sight extinction estimate, which they estimated to be larger than $E(B-V) = 0.4$ mag at the 2σ level and larger than $E(B-V) = 0.8$ mag at the 1σ level. Van Dyk et al. (2012) conducted a similar analysis, where they carefully discussed the infrared photometric calibration and the subtle effects due to the progenitor *pre-explosion* reddening (which they estimated as $E(B-V) = 0.71$ mag) and the variability of the RSG. They found the spectral energy distribution (SED) to be consistent with an effective temperature of 3600 K, a luminosity $L \sim 10^{5.21}\,L_\odot$, a radius $R = 1040\,R_\odot$, and an initial mass between 15 and $20\,M_\odot$. After interpolating their adopted tracks (taken from Ekström et al. 2012), they finally constrained the progenitor initial mass to be $\sim$17–$18\,M_\odot$, which is at the upper end of the initial masses for the Type IIP SNe progenitors detected to date, as suggested by Smartt et al. (2009). Subsequently, Kochanek et al. (2012) suggested that the Fraser et al. (2012a) and the Van Dyk et al. (2012) progenitor luminosity (and mass) values may have been overestimated, since they adopted for the reddening the classical absorption-to-reddening ratio $R_V = 3.1$, which is appropriate for a standard dust composition (Cardelli et al. 1989). Kochanek et al. (2012) pointed out that a massive RSG produces mostly silicates, for which a ratio of $R_V = 2$ is more appropriate. Moreover, visual extinction may be overestimated, since the contribution of the scattered light in the interstellar extinction budget is neglected. In turn, they suggested a progenitor luminosity between $L = 10^{4.8}\,L_\odot$ and $L = 10^{5.0}\,L_\odot$ and a mass $M < 15\,M_\odot$.

Accurate *BVRI* light curves of SN 2012aw were published by Munari et al. (2013), who carefully discussed the problems related to the homogenization of photometric measurements obtained at different telescopes, producing an optimal light curve by means of their "lightcurve merging method." Moreover, extensive photometric and spectroscopic observations were presented by Bose et al. (2013), covering a period from 4 to 270 days after explosion. Bose et al. (2013) measured the photospheric velocity, the temperature, and the ^{56}Ni mass of SN 2012aw; they estimated the explosion energy and the mass of the progenitor star by comparing their data with existing simulations.

In this paper, we present the results of our observational campaign, which include unpublished near-infrared data. We used our data for *new* hydrodynamical simulations to estimate the relevant physical parameters. The same approach has been used for other two Type IIP SNe, namely SN 2012A (Tomasella et al. 2013) and SN 2012ec (C. Barbarino et al. 2014, in preparation), thus providing a homogeneous analysis that can be used for consistent comparisons.

The paper is organized as follows. In Section 2, we list the relevant properties of the host galaxy M95. In Section 3, we

discuss the reddening estimate, both Galactic and host. In Section 4, we present our photometric data set and analyze the photometric time evolution. In Section 5, we present the spectroscopic observations and discuss the time evolution of the spectral features. In Section 6, we discuss the physical parameters obtained from the photometric and spectroscopic data: the bolometric light curve, from which we give an estimate of the ^{56}Ni mass, the expansion velocity of the ejecta, and SED evolution. In Section 7, we present the results of our hydrodynamical modeling, computed to match the observational parameters of SN 2012aw. Conclusions are presented in Section 8.

2. THE HOST GALAXY M95

M95 (NGC 3351, $\alpha_{2000} = 10^{h}43^{m}57^{s}.7$, $\delta_{2000} = 11^{o}42'12''.7$) is a face-on SBb(r)II spiral galaxy (Sandage & Tammann 1987) belonging to the Leo I Group. The total V-band magnitude is $M_V = -20.61 \pm 0.09$ mag and the total baryonic mass has been estimated as $M_{\rm tot} = (3.57 \pm 0.30) \times 10^{10}\, M_{\odot}$ (Gurovich et al. 2010). The distance to M95 has been estimated with Cepheids and the tip of the red giant branch (TRGB). A range of distances have been reported over many years, but the latest estimates are comfortably converging: the HST Key Project gave a Cepheids-based distance of $(m - M)_0 = 30.00 \pm 0.09$ mag (Freedman et al. 2001), in excellent agreement with the TRGB-based distance of $(m - M)_0 = 29.92 \pm 0.05$ mag (Rizzi et al. 2007). This agreement is particularly striking, since it is based on two truly independent distance indicators, as Cepheids are young Population I stars, while the TRGB is a feature of the old Population II. A similar distance modulus was also obtained on the basis of the planetary nebulae luminosity function ($(m - M)_0 = 30.0 \pm 0.16$ mag, Ciardullo et al. 2002). In the following, we will adopt as a distance modulus $(m - M)_0 = 29.96 \pm 0.04$ mag, which is the average of the Cepheids- and TRGB-based distances. M95 is known to host a central massive black hole (e.g., Beifiori et al. 2009), and its bulge shows intense star forming activity (e.g., Hägele et al. 2007). SN 2012aw is located in a southern outer arm, 60″ west and 115″ south of the center of M95. The metallicity at the SN position can be approximated as solar-like (Fraser et al. 2012a). To our knowledge, no SN events were recorded in M95 before SN 2012aw. Last, we note that the redshift of M95, as measured from the H I 21 cm line, is $z = 0.002598 \pm 0.000002$ (Springbob et al. 2005): we have adopted this value to redshift correct our spectra.

3. REDDENING

In order to evaluate the physical parameters of the SN, photometric and spectroscopic data must be corrected for both the Galactic and the host galaxy reddening and for the distance. The Galactic reddening was estimated using the Schlegel et al. (1998) maps, yielding $E(B - V) = 0.028$ mag. We note that the new calibration of the dust maps, provided by Schlafly & Finkbeiner (2011), gives $E(B - V) = 0.024$ mag. In the following discussion, we will adopt $E(B - V) = 0.028$ mag for the Galactic reddening.

The host galaxy reddening was estimated on the basis of the Na ID equivalent width (EW) extracted from a SARG high-resolution spectrum. We measured EW(D2 λ5891) = 286 ± 17 mÅ and EW(D1 λ5897) = 240 ± 16 mÅ, corresponding to a column density of log(Na I) = 12.80 ± 0.14. As a first attempt, we used a classical (but still widely adopted in the literature; see, for example, Liszt 2014) route to the reddening estimate: following Ferlet et al. (1985), the Na I column density value translates into $\log(H) = 21.05 \pm 0.14$ and, according to Bohlin et al. (1978), into a color excess of $E(B - V)_{\rm host} = 0.19^{\pm 0.15}_{\pm 0.09}$ mag. The quoted uncertainty takes into account the 30% uncertainty of the Bohlin et al. (1978) calibration only. This transforms into a relatively high host absorption of $A(B)_{\rm host} = 0.79^{\pm 0.62}_{\pm 0.37}$ mag, if a Galactic $R_V = 3.1$ total-to-selective absorption ratio (Cardelli et al. 1989) is assumed. We note that this large (but rather uncertain) value is in agreement, with the $E(B - V) = 0.15$ mag upper limit given by Bose et al. (2013), on the basis of a blackbody fit to the early observed fluxes. Interestingly, by adopting the calibration given by Turatto et al. (2003) with the EW measured on the low-resolution spectra of Bose et al. (2013), we get $E(B - V)_{\rm host} = 0.16$ mag. This reddening value is also in good agreement with the Munari & Zwitter (1997) calibration (their Table 2), which suggests a reddening in the range $E(B - V)_{\rm host} = 0.10$–$0.12$ mag.

As an independent check, we used the "color-method" (Olivares et al. 2010). This method relies on the assumption that, at the end of the plateau, the intrinsic $(V - I)$ color is constant, and a possible color-excess is only due to the host galaxy reddening (after correcting for the Galactic reddening). According to their Equation (7),

$$A_V(V - I) = 2.518[(V - I) - 0.656] \quad (1)$$

$$\sigma(A_V) = 2.518\sqrt{\sigma_{(V-I)} + 0.053^2 + 0.059^2}, \quad (2)$$

and following the prescriptions described in their paper, in the above formulae we adopted the $(V - I)$ color at day ∼94, corrected for the foreground extinction, which is roughly 15 days before the end of the plateau. We derive $A(V)_{\rm host} = (0.44 \pm 0.10)$ mag, which corresponds to $E(B - V) = 0.14 \pm 0.03$ mag (Cardelli et al. 1989), in agreement with the other quoted estimates.

It is interesting to note that our EW(Na ID) measurements are, within the uncertainties, in excellent agreement with those obtained by Van Dyk et al. (2012), of $EW(D2) = 269 \pm 14$ Å and $EW(D1) = 231 \pm 11$ Å. Van Dyk et al. (2012) derived a significantly lower reddening, of $E(B - V)_{\rm host} = 0.055 \pm 0.014$ mag, by adopting the precise Poznanski et al. (2012) calibration. Consistently, Bose et al. (2013) obtained with the same method $E(B-V)_{\rm host} = 0.041 \pm 0.011$ mag. These values are lower than those based on the other quoted methods, which point toward a reddening of $E(B - V) \sim 0.14$ mag. Interestingly, the latter value is consistent with the new $N(\mathrm{H\,I})/E(B - V)$ calibration provided by Liszt (2014), which gives $E(B - V) = 0.13$ mag (for the sake of completeness, this calibration is referred to the relationship between the reddening and the atomic hydrogen column density only). However, both the Bohlin et al. (1978) and the Liszt (2014) calibrations need an intermediate step to transform the Na I column density into H column density, which adds its own uncertainty to the final estimate.

Therefore, we decided to follow our referee's suggestion to adopt the direct calibration of the reddening from the Na I column density provided by Poznanski et al. (2012), from which we get $E(B-V)_{\rm host} = 0.058 \pm 0.016$ mag. This value translates into $A(B)_{\rm host} = 0.24 \pm 0.07$ mag. For the following discussion, we will adopt a total extinction of $A(B)_{\rm tot} = 0.36 \pm 0.07$ mag.

4. PHOTOMETRY

4.1. Data

An intensive campaign of optical and near-infrared (NIR) observations of SN 2012aw was promptly started after its discovery (2012 March 17, day 0), and lasted until the end of the plateau and the beginning of the radioactive tail phase (2012 July 21, day 130), when the SN went into conjunction with the Sun. Two additional epochs were collected on 2012 December 26 and on 2013 February 11 (day 286 and day 333, respectively), well into the nebular phase.

Optical *UBVRI* Johnson–Cousins images were collected with the 67/92 cm Asiago Schmidt Telescope (Italy), equipped with an SBIG STL-11000M CCD camera (13 epochs), the array of 0.41 m Panchromatic Robotic Optical Monitoring and Polarimetry Telescopes (PROMPT, Chile), equipped with Apogee U47p cameras, which employ the E2V CCDs (33 epochs), the 2.2 m telescope at the Calar Alto Observatory (Spain), equipped with the CAFOS Focal Reducer and Faint Object Spectrograph instrument (2 epochs), the 1.82m Copernico telescope at Cima Ekar (Italy), equipped with the AFOSC Asiago Faint Object Spectrograph and Camera (2 epochs), the ESO NTT telescope (Chile), equipped with the EFOSC2 ESO Faint Object Spectrograph and Camera (2 epochs), the 4.2 m William Herschel Telescope (WHT; Canary Islands, Spain), equipped with the ACAM Auxiliary Port Camera (2 epochs), and the 2.5 m Nordic Optical Telescope (Canary Islands, Spain), equipped with the ALFOSC Andalucia Faint Object Spectrograph and Camera (3 epochs). Two early epochs, collected during the rise of the light curve and discussed in Munari et al. (2013), have been included in our analysis for a better sampling of these phases.

Optical *ugriz* Sloan data were collected with the PROMPT Telescopes (21 epochs), the 2.0 m Liverpool Telescope (LT, Canary Islands, Spain), equipped with the RATCam optical CCD camera (11 epochs), and the 2.0 m Faulkes Telescope North (Hawaii, USA), equipped with the FI CCD486 CCD detector (4 epochs).

NIR *JHK* data were obtained with the 0.6m Rapid Eye Mount (REM) Telescope (Chile), equipped with the REMIR infrared camera (11 epochs), the 1.52 m Carlos Sanchez Telescope (TCS; Canary Islands, Spain), equipped with the CAIN infrared camera (8 epochs), and the 3.58 m Telescopio Nazionale Galileo (G, Canary Islands, Spain), equipped with the NICS Near Infrared Camera Spectrometer (1 epoch).

In summary, our photometry densely covers the photospheric phase in the *UBVRI* and in *ugriz* photometric systems, with 58 epochs ranging from day 1.9 to day 130, and with 30 epochs from day 3.1 to day 114, respectively. Moreover, two additional epochs have been collected in *UBVRI* during the nebular phase. Our NIR data are the only currently available in the literature for SN 2012aw, and they cover 17 epochs from day 7.6 to day 94.

Data were pre-reduced by the instruments pipelines, when available, or with standard procedures (bias and flat-field corrections, trimming; plus background subtraction for the NIR data) in the IRAF[21] environment. In a few cases, in which the sky background subtraction was not satisfactory, some NIR images were pre-reduced by means of an IRAF-based custom pipeline, which adopts for the background subtraction a two-step technique based on a preliminary guess of the sky background and on a careful masking of unwanted sources in the sky images, by means of the XDIMSUM IRAF package (Coppola et al. 2011).

Photometric measurements were carried out with the QUBA pipeline (Valenti et al. 2011), which performs point-spread function (PSF) photometry on the SN and on selected field stars. Johnson–Cousins *UBVRI* magnitudes of the reference stars were calibrated by averaging the photometric sequence published in Henden et al. (2012) and our measurements obtained with the 67/92 cm Asiago Schmidt Telescope; Sloan *ugriz* reference star magnitudes were calibrated using images taken at the LT, during selected photometric nights. We did not transform the *ugriz* data set into the *UBVRI* system, because the current state-of-the-art transformations (Jordi et al. 2006), which are appropriate for normal field stars, may not be accurate for SNe whose SED is strongly dominated by intense absorptions and emissions, which significantly alter the blackbody energy distribution.[22] Four reference stars in the *UBVRI* system (namely, IDs 1, 2, 3, and 7) are in common with Bose et al. (2013): the differences in the photometry are -0.020 ± 0.052 mag, -0.007 ± 0.037 mag, 0.012 ± 0.035 mag, -0.002 ± 0.059 mag, and -0.001 ± 0.023 mag in the *U*, *B*, *V*, *R*, and *I* bands, respectively. Reference stars 1 and 2 also have Sloan Digital Sky Survey Data Release 9 (SDSS DR9; Ahn et al. 2012 measurements): the differences are 0.026 ± 0.045 mag, 0.028 ± 0.024 mag, -0.008 ± 0.012 mag, 0.010 ± 0.008 mag, and 0.022 ± 0.002 mag, in the *u*, *g*, *r*, *i*, and *z* bands, respectively. We point out that our adopted reference stars showed no clear signs of variability.

NIR data were calibrated by reference to four well measured Two Micron All Sky Survey (2MASS; Skrutskie et al. 2006) reference stars. We did not correct for the color terms, since they are generally very small in the NIR bands (e.g., Carpenter 2001) and the uncertainties of the photometric measurements were significantly larger than those related to neglecting the color terms. Because of the small field of view, only one reference star was available in TCS images, and it was not possible to produce an accurate PSF model. We therefore adopted aperture photometry. However, we explicitly note that the SN is located far from the host galaxy's inner regions, and we do not expect a significant contamination of the background by the host galaxy.

Table 1 lists the positions and the photometric properties of the adopted reference stars, while a map of SN 2012aw and of the reference stars is shown in Figure 1. The photometry of SN 2012aw is reported in Tables 2, 3, and 4 for the *UBVRI*, *ugriz*, and *JHK* systems, respectively. Reported photometric uncertainties are computed using the photometric errors and the uncertainties in the calibrations. When multiple exposures were available in the same night for the same filter, the adopted error was the rms of the measured magnitudes.

4.2. Time Evolution

We were able to follow the photospheric phase of SN 2012aw up to day ∼130, observing the end of the plateau phase. Figures 2, 3, and 4 show the photometric evolution of SN 2012aw in the Johnson–Cousins, Sloan, and NIR photometric systems, respectively. Figure 5 shows a close-up of the *V*, *R*, and *I* light curves in the first ∼120 days. Error bars are typically smaller than the symbol size, except for the NIR plot.

[21] IRAF is distributed by the National Optical Astronomical Observatory, which is operated by the Association of Universities for Research in Astronomy, Inc., under cooperative agreement with the National Science Foundation.

[22] The transformations between these two photometric systems may lead to systematic errors in the $u - g$ color even for normal field stars, as the $u - g$ color is particularly sensitive to temperature, surface gravity, and metallicity (e.g., Lenz et al. 1998).

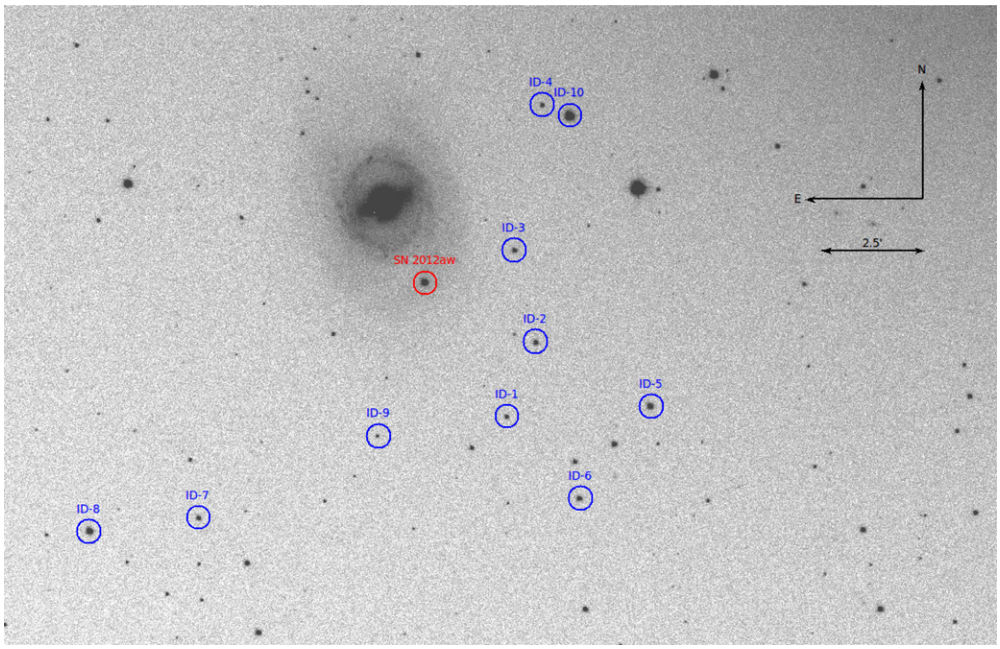

Figure 1. Finding chart of SN 2012aw and the reference stars. *V*-band image collected at the 67/92 cm Asiago Schmidt Telescope on 2012 March 20. The area shown here is approximately 24 × 15 arcmin^2.

(A color version of this figure is available in the online journal.)

Table 1
Positions and Photometry of the Selected Reference Stars

Star ID	$\alpha_{J2000.0}$ (deg)	$\delta_{J2000.0}$ (deg)	U (mag)	B (mag)	V (mag)	R (mag)	I mag
1	160.94117	11.617182		16.384 ± 0.018	15.620 ± 0.006	15.076 ± 0.009	14.694 ± 0.013
2	160.92930	11.647304	15.729 ± 0.008	15.613 ± 0.012	14.853 ± 0.020	14.416 ± 0.020	14.018 ± 0.020
3	160.93780	11.684113	15.221 ± 0.009	15.351 ± 0.040	14.972 ± 0.028	14.706 ± 0.026	14.450 ± 0.012
4	160.92599	11.743191		17.116 ± 0.012	15.821 ± 0.005	14.952 ± 0.006	14.104 ± 0.030
5	160.88154	11.620989		14.992 ± 0.026	13.932 ± 0.038	13.248 ± 0.028	12.717 ± 0.034
6	160.91103	11.583979		15.551 ± 0.018	14.669 ± 0.020	14.145 ± 0.012	13.670 ± 0.002
7	161.06876	11.576971		15.706 ± 0.009	14.873 ± 0.034	14.334 ± 0.019	13.949 ± 0.004
8	161.11392	11.571762		14.249 ± 0.022	13.516 ± 0.029	13.088 ± 0.026	12.718 ± 0.025
Star ID	$\alpha_{J2000.0}$ (deg)	$\delta_{J2000.0}$ (deg)	u (mag)	g (mag)	r (mag)	i (mag)	z mag
1	160.94117	11.617182		15.967 ± 0.024	15.372 ± 0.021	15.168 ± 0.015	15.105 ± 0.018
2	160.92930	11.647304	16.612 ± 0.044	15.244 ± 0.018	14.653 ± 0.016	14.433 ± 0.008	14.312 ± 0.012
3	160.93780	11.684113	16.092 ± 0.029	15.108 ± 0.018	14.883 ± 0.016	14.823 ± 0.012	14.830 ± 0.021
Star ID	$\alpha_{J2000.0}$ (deg)	$\delta_{J2000.0}$ (deg)	J (mag)	H (mag)	K (mag)		
2	160.92930	11.647304	13.380 ± 0.027	13.025 ± 0.026	12.914 ± 0.034		
4	160.94117	11.617182	13.163 ± 0.026	12.476 ± 0.024	12.347 ± 0.031		
9	160.93780	11.684113	12.816 ± 0.024	12.218 ± 0.024	12.001 ± 0.021		
10	160.91448	11.738809	10.233 ± 0.027	9.741 ± 0.026	9.554 ± 0.027		

Notes. *UBVRI* and *ugriz* magnitudes have been calibrated with Landolt fields on photometric nights; *JHK* magnitudes have been taken from the 2MASS catalog. Star IDs are the same for the three systems.

Solid curves represent Chebyshev polynomials fitted to the observed data points, with the `CURFIT` `IRAF` task. The order of the fit was allowed to vary to minimize the χ^2. The rms was generally of the order of ∼0.03 mag. In a few cases (*U*, *u*, and NIR bands) the sampling was poor and we adopted a cubic spline. The last two points, collected in the SN nebular phase, were not included in the fit. The plotted light curves show that the SN was discovered well before the *V*-band maximum, estimated from the fit at Julian Day 2, 456, 011.8 ± 0.5 (day 9.3 ± 0.5). A comparison of the early spectra of SN 2012aw (see Section 5.2) with the collection of spectra available through the web tool `GELATO` (Harutyunyan et al. 2008) independently confirms our estimate of the epoch of the explosion. The Johnson *U* and *B* light curves show a steady decline from day 2 and day ∼7 onward, respectively, whereas *V*, *R*, and *I* bands show the typical plateau behavior of Type IIP events. The plateau lasts for ∼100 days (also confirmed in Bose et al. 2013), followed by the drop to the radioactive tail. The Sloan photometry is consistent

Table 2
Log of *UBVRI* Photometric Observations of SN 2012aw

Date	JD (2400000+)	Phase[a] (days)	*U* (mag)	*B* (mag)	*V* (mag)	*R* (mag)	*I* (mag)	Source[b]
17/03/2012	56004.41	1.9		13.79 ± 0.01	13.86 ± 0.01	13.82 ± 0.01	13.72 ± 0.01	1
18/03/2012	56005.57	3.1		13.52 ± 0.05	13.68 ± 0.05	13.53 ± 0.03	13.53 ± 0.01	12
19/03/2012	56006.71	4.2		13.47 ± 0.12	13.59 ± 0.11	13.40 ± 0.09	13.39 ± 0.07	12
19/03/2012	56006.41	3.9		13.60 ± 0.01	13.58 ± 0.01	13.43 ± 0.01	13.31 ± 0.01	1
19/03/2012	56006.44	3.9		13.54 ± 0.08	13.56 ± 0.07	13.35 ± 0.05	13.41 ± 0.05	2
20/03/2012	56007.57	5.1		13.47 ± 0.11	13.52 ± 0.10	13.29 ± 0.08	13.28 ± 0.06	12
20/03/2012	56007.31	4.8		13.53 ± 0.06	13.52 ± 0.06	13.38 ± 0.05	13.39 ± 0.05	2
21/03/2012	56008.57	6.1		13.38 ± 0.05	13.39 ± 0.05	13.22 ± 0.03	13.20 ± 0.04	12
21/03/2012	56008.31	5.8		13.41 ± 0.05	13.44 ± 0.05	13.27 ± 0.06	13.22 ± 0.05	2
22/03/2012	56009.58	7.1		13.42 ± 0.02	13.38 ± 0.02	13.11 ± 0.04	13.13 ± 0.03	12
22/03/2012	56009.31	6.8		13.42 ± 0.04	13.36 ± 0.04	13.19 ± 0.04	13.16 ± 0.02	2
23/03/2012	56010.54	8.0		13.36 ± 0.02	13.34 ± 0.02	13.11 ± 0.03	13.11 ± 0.02	12
23/03/2012	56010.35	7.8		13.43 ± 0.02	13.34 ± 0.02	13.18 ± 0.03	13.11 ± 0.01	2
23/03/2012	56010.35	7.8	12.50 ± 0.04	13.35 ± 0.02	13.30 ± 0.02	13.10 ± 0.01	13.07 ± 0.03	3
23/03/2012	56010.36	7.9		13.39 ± 0.03	13.30 ± 0.03	13.12 ± 0.01	13.12 ± 0.01	2
24/03/2012	56011.54	9.0		13.38 ± 0.03	13.28 ± 0.03	13.11 ± 0.02	13.07 ± 0.02	12
24/03/2012	56011.36	8.9	12.55 ± 0.08	13.32 ± 0.03	13.29 ± 0.02	13.12 ± 0.02	13.06 ± 0.03	3
26/03/2012	56013.36	10.9	12.74 ± 0.07	13.43 ± 0.06				5
26/03/2012	56013.39	10.9			13.33 ± 0.03	13.16 ± 0.04	13.08 ± 0.03	2
27/03/2012	56014.44	11.9		13.43 ± 0.03	13.31 ± 0.03			2
28/03/2012	56015.53	13.0		13.51 ± 0.04	13.35 ± 0.03	13.13 ± 0.02	13.07 ± 0.02	12
28/03/2012	56015.39	12.9	12.84 ± 0.06	13.50 ± 0.02	13.35 ± 0.02	13.12 ± 0.02	13.07 ± 0.05	5
29/03/2012	56016.51	14.0		13.48 ± 0.02	13.35 ± 0.02	13.11 ± 0.02	13.03 ± 0.04	12
29/03/2012	56016.37	13.9		13.46 ± 0.03	13.30 ± 0.03	13.12 ± 0.03	13.01 ± 0.01	2
30/03/2012	56017.57	15.1		13.61 ± 0.09	13.34 ± 0.08	13.14 ± 0.03	12.98 ± 0.03	12
30/03/2012	56017.37	14.9				13.08 ± 0.02	13.02 ± 0.03	12
31/03/2012	56018.43	15.9		13.53 ± 0.02	13.29 ± 0.02	13.13 ± 0.03	12.98 ± 0.02	2
02/04/2012	56020.32	17.8		13.58 ± 0.07	13.34 ± 0.06	13.13 ± 0.05	12.92 ± 0.03	2
11/04/2012	56029.53	27.0			13.37 ± 0.06	13.06 ± 0.08	12.90 ± 0.03	12
14/04/2012	56032.60	30.1			13.40 ± 0.01	13.05 ± 0.01	12.90 ± 0.05	12
17/04/2012	56035.55	33.0			13.44 ± 0.02	13.09 ± 0.01	12.88 ± 0.01	12
24/04/2012	56042.43	39.9		14.41 ± 0.03	13.42 ± 0.02	13.13 ± 0.03	12.86 ± 0.02	2
25/04/2012	56043.40	40.9		14.41 ± 0.04	13.44 ± 0.04	13.08 ± 0.03	12.84 ± 0.04	2
25/04/2012	56043.49	41.0		14.43 ± 0.01	13.45 ± 0.01	13.06 ± 0.03	12.91 ± 0.04	7
30/04/2012	56048.55	46.0	15.43 ± 0.02	14.45 ± 0.02	13.46 ± 0.02	13.07 ± 0.02	12.84 ± 0.02	6
02/05/2012	56049.94	47.4			13.50 ± 0.02	13.05 ± 0.03	12.80 ± 0.04	12
03/05/2012	56050.57	48.1		14.54 ± 0.04	13.46 ± 0.04	13.07 ± 0.04	12.79 ± 0.03	12
06/05/2012	56053.40	50.9	15.70 ± 0.03	14.72 ± 0.02	13.54 ± 0.02	13.07 ± 0.04	12.82 ± 0.05	13
09/05/2012	56056.61	54.1			13.53 ± 0.02	13.08 ± 0.03	12.81 ± 0.02	12
12/05/2012	56059.65	57.2		14.71 ± 0.08	13.53 ± 0.08	13.10 ± 0.04	12.80 ± 0.01	12
21/05/2012	56069.55	67.0		15.10 ± 0.06	13.56 ± 0.05	13.02 ± 0.03	12.76 ± 0.03	12
23/05/2012	56071.57	69.1			13.59 ± 0.03	13.02 ± 0.04	12.90 ± 0.04	12
26/05/2012	56074.38	71.9	16.56 ± 0.05	14.97 ± 0.01	13.60 ± 0.01	13.08 ± 0.02	12.83 ± 0.02	7
27/05/2012	56075.61	73.1			13.59 ± 0.02	13.02 ± 0.03	12.75 ± 0.03	12
07/06/2012	56086.55	84.0			13.64 ± 0.01	13.11 ± 0.01		12
13/06/2012	56092.51	90.0			13.67 ± 0.03	13.11 ± 0.03		12
17/06/2012	56096.41	93.9	17.17 ± 0.06	15.19 ± 0.02	13.75 ± 0.02	13.17 ± 0.01	12.88 ± 0.01	7
24/06/2012	56103.53	101.0			13.82 ± 0.04	13.18 ± 0.05	12.88 ± 0.04	12
26/06/2012	56105.40	102.9		15.45 ± 0.04	13.88 ± 0.02	13.21 ± 0.04	12.85 ± 0.06	13
02/07/2012	56111.48	109.0		15.31 ± 0.12	13.90 ± 0.11	13.29 ± 0.05	12.95 ± 0.03	12
06/07/2012	56115.49	113.0		15.45 ± 0.04	14.01 ± 0.03	13.37 ± 0.05	13.08 ± 0.06	12
07/07/2012	56116.40	113.9	17.62 ± 0.05	15.47 ± 0.03	14.03 ± 0.03	13.40 ± 0.02	13.11 ± 0.02	7
08/07/2012	56117.48	115.0		15.49 ± 0.11	14.02 ± 0.10	13.40 ± 0.02	13.12 ± 0.02	12
09/07/2012	56118.49	116.0		15.52 ± 0.05	14.05 ± 0.05	13.37 ± 0.03	13.08 ± 0.02	12
17/07/2012	56126.48	123.0		15.87 ± 0.07	14.32 ± 0.03	13.63 ± 0.03	13.28 ± 0.03	12
19/07/2012	56128.48	126.0		15.92 ± 0.12	14.46 ± 0.11			12
20/07/2012	56129.48	127.0				13.88 ± 0.04	13.57 ± 0.05	12
23/07/2012	56132.47	130.0			14.67 ± 0.01	13.88 ± 0.02		12
26/12/2013	56288.70	286.2		18.55 ± 0.02	17.37 ± 0.02	16.36 ± 0.04	15.90 ± 0.03	7
11/02/2013	56335.63	333.1	20.34 ± 0.10	18.98 ± 0.03	17.80 ± 0.02	16.85 ± 0.01	16.32 ± 0.02	13

Notes. See the text for details on the individuals instruments.
[a] JD − 2,450,002.5.
[b] 1 = Munari; 2 = Asiago Schmidt Telescope; 3 = CAFOS; 5 = AFOSC; 6 = EFOSC2; 7 = ALFOSC; 12 = PROMPT; 13 = ACAM.

Table 3
Log of *ugriz* Photometric Observations of SN 2012aw

Date	JD (2400000+)	Phase[a] (days)	u (mag)	g (mag)	r (mag)	i (mag)	z (mag)	Source[b]
18/03/2012	56005.57	3.1		13.57 ± 0.04	13.68 ± 0.03	13.87 ± 0.02	14.00 ± 0.02	12
19/03/2012	56006.58	4.1		13.46 ± 0.03	13.57 ± 0.02	13.73 ± 0.01	13.84 ± 0.01	12
20/03/2012	56007.57	5.1		13.50 ± 0.04	13.46 ± 0.03	13.62 ± 0.01	13.75 ± 0.02	12
21/03/2012	56008.57	6.1	13.34 ± 0.11	13.40 ± 0.03	13.38 ± 0.02	13.54 ± 0.02	13.67 ± 0.02	12
22/03/2012	56009.58	7.1		13.38 ± 0.03	13.32 ± 0.02	13.49 ± 0.01	13.62 ± 0.02	12
23/03/2012	56010.54	8.0		13.33 ± 0.02	13.31 ± 0.02	13.47 ± 0.01	13.58 ± 0.02	12
23/03/2012	56010.36	7.9	13.29 ± 0.04	13.26 ± 0.03	13.30 ± 0.02	13.43 ± 0.01	13.52 ± 0.01	2
24/03/2012	56011.54	9.0		13.33 ± 0.03	13.28 ± 0.03	13.41 ± 0.01	13.54 ± 0.02	12
25/03/2012	56012.06	9.6		13.30 ± 0.12	13.24 ± 0.13	13.45 ± 0.04	13.54 ± 0.07	10
26/03/2012	56013.49	11.0	13.55 ± 0.14	13.27 ± 0.02	13.26 ± 0.01	13.40 ± 0.02	13.49 ± 0.02	4
28/03/2012	56015.53	13.0		13.38 ± 0.05	13.29 ± 0.05	13.38 ± 0.01	13.47 ± 0.02	12
29/03/2012	56016.51	14.0		13.37 ± 0.04	13.27 ± 0.03	13.40 ± 0.02	13.50 ± 0.02	12
30/03/2012	56017.37	14.9		13.34 ± 0.11	13.32 ± 0.10	13.37 ± 0.03	13.43 ± 0.02	12
06/04/2012	56024.41	21.9	14.39 ± 0.06	13.42 ± 0.02	13.18 ± 0.02	13.26 ± 0.03	13.28 ± 0.01	4
11/04/2012	56029.53	27.0			13.21 ± 0.01	13.28 ± 0.01	13.34 ± 0.01	12
14/04/2012	56032.60	30.1			13.24 ± 0.02	13.29 ± 0.02	13.27 ± 0.03	12
16/04/2012	56034.56	32.1		13.76 ± 0.04	13.21 ± 0.04	13.26 ± 0.01		4
17/04/2012	56035.55	33.0			13.25 ± 0.02	13.31 ± 0.03	13.26 ± 0.01	12
21/04/2012	56039.41	36.9	16.18 ± 0.08	13.82 ± 0.01	13.25 ± 0.01	13.27 ± 0.02	13.24 ± 0.01	4
09/05/2012	56056.61	54.1			13.27 ± 0.02	13.23 ± 0.02	13.14 ± 0.02	12
14/05/2012	56061.58	59.1		14.11 ± 0.03	13.26 ± 0.03	13.21 ± 0.02	13.12 ± 0.01	12
21/05/2012	56069.55	67.0			13.27 ± 0.02	13.22 ± 0.02	13.04 ± 0.04	12
23/05/2012	56071.57	69.1			13.30 ± 0.01	13.22 ± 0.01		12
26/05/2012	56074.43	71.9	17.67 ± 0.16	14.22 ± 0.02	13.27 ± 0.02	13.19 ± 0.01	13.10 ± 0.01	4
27/05/2012	56075.61	73.1			13.27 ± 0.02		13.11 ± 0.02	12
31/05/2012	56079.41	76.9	17.90 ± 0.12	14.22 ± 0.03	13.30 ± 0.02	13.20 ± 0.02	13.11 ± 0.02	4
01/06/2012	56080.41	77.9	17.84 ± 0.10	14.26 ± 0.03	13.27 ± 0.03	13.21 ± 0.02	13.09 ± 0.02	4
07/06/2012	56086.55	84.0			13.29 ± 0.03	13.29 ± 0.03	13.21 ± 0.06	12
24/06/2012	56103.53	101.0			13.42 ± 0.02	13.36 ± 0.02	13.23 ± 0.02	12
07/07/2012	56116.48	114.0			13.62 ± 0.02	13.54 ± 0.02	13.36 ± 0.01	12

Notes. See the text for details on the individual instruments.
[a] JD − 2,450,002.5.
[b] 2 = Asiago Schmidt Telescope; 4 = RATCAM; 10 = Faulkes North; 12 = PROMPT.

Table 4
Log of NIR Observations of the SN 2012aw

Date	JD (2400000+)	Phase[a] (days)	J (mag)	H (mag)	K (mag)	Source[b]
23/03/2012	56010.07	7.6	13.00 ± 0.06	12.95 ± 0.06	12.66 ± 0.06	9
24/03/2012	56011.09	8.6	13.04 ± 0.04	12.87 ± 0.04	12.71 ± 0.07	9
25/03/2012	56012.12	9.6	12.90 ± 0.04	12.78 ± 0.04	12.52 ± 0.04	9
29/03/2012	56016.68	14.2	12.82 ± 0.10	12.63 ± 0.07	12.45 ± 0.06	8
01/04/2012	56019.07	16.6	12.80 ± 0.04	12.62 ± 0.04	12.56 ± 0.04	9
04/04/2012	56022.08	19.6	12.74 ± 0.03	12.57 ± 0.03	12.42 ± 0.04	9
07/04/2012	56025.07	22.6		12.55 ± 0.08	12.35 ± 0.04	9
13/04/2012	56031.37	28.9	12.56 ± 0.07	12.39 ± 0.08		11
17/04/2012	56035.01	32.5	12.54 ± 0.05	12.34 ± 0.05	12.26 ± 0.04	9
22/04/2012	56040.38	37.9			11.96 ± 0.17	11
24/04/2012	56042.12	39.6	12.49 ± 0.09	12.34 ± 0.09	12.14 ± 0.09	9
02/05/2012	56049.99	47.5	12.41 ± 0.04	12.21 ± 0.04	12.08 ± 0.06	9
04/05/2012	56052.42	49.9	12.34 ± 0.04	12.03 ± 0.06		11
15/05/2012	56063.41	60.9	12.49 ± 0.04	12.74 ± 0.07		11
06/06/2012	56085.40	82.9	12.31 ± 0.02	12.18 ± 0.06		11
10/06/2012	56088.41	85.9	12.34 ± 0.04	12.12 ± 0.04	11.97 ± 0.11	11
17/06/2012	56096.44	93.9	12.42 ± 0.03	12.23 ± 0.06	12.04 ± 0.01	11

Notes. See the text for details on the individual instruments.
[a] JD − 2,450,002.5.
[b] 8 = NICS; 9 = REM; 11 = TCS.

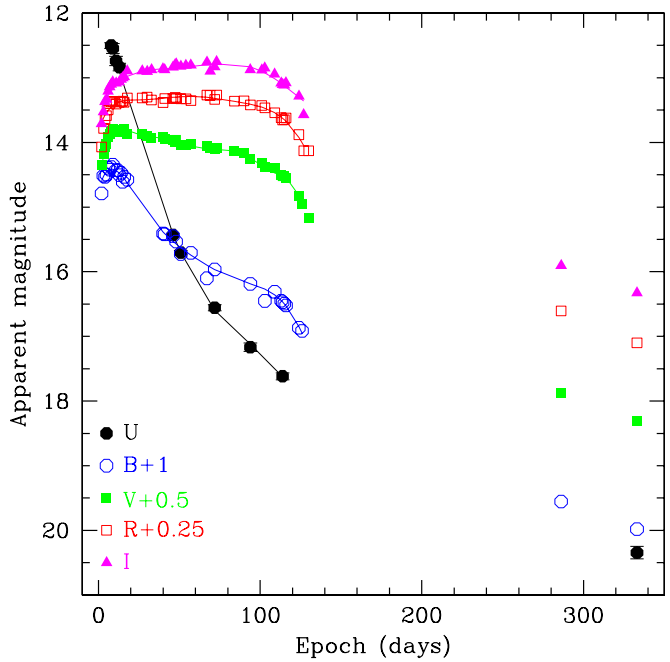

Figure 2. Photometric evolution in the *UBVRI* system. Individual light curves were shifted for clarity. Day 0 corresponds to the adopted explosion epoch.
(A color version of this figure is available in the online journal.)

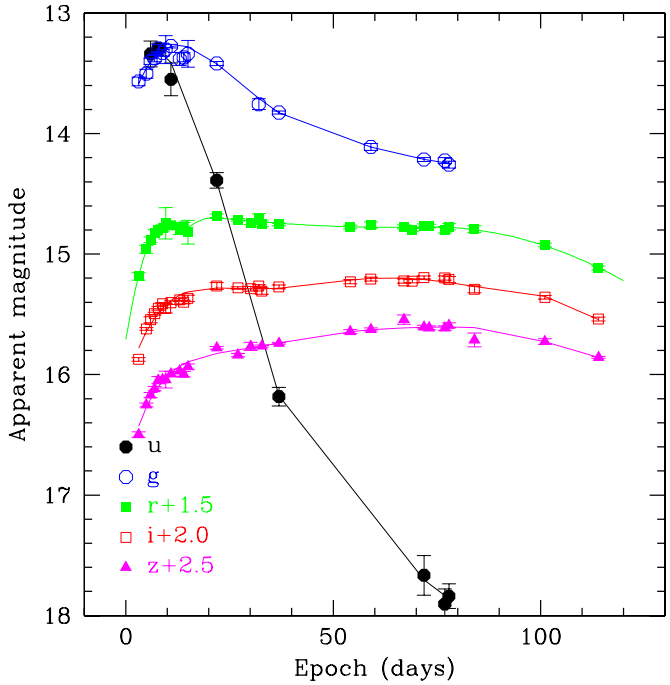

Figure 3. Photometric evolution in the *ugriz* system. Individual light curves were shifted for clarity.
(A color version of this figure is available in the online journal.)

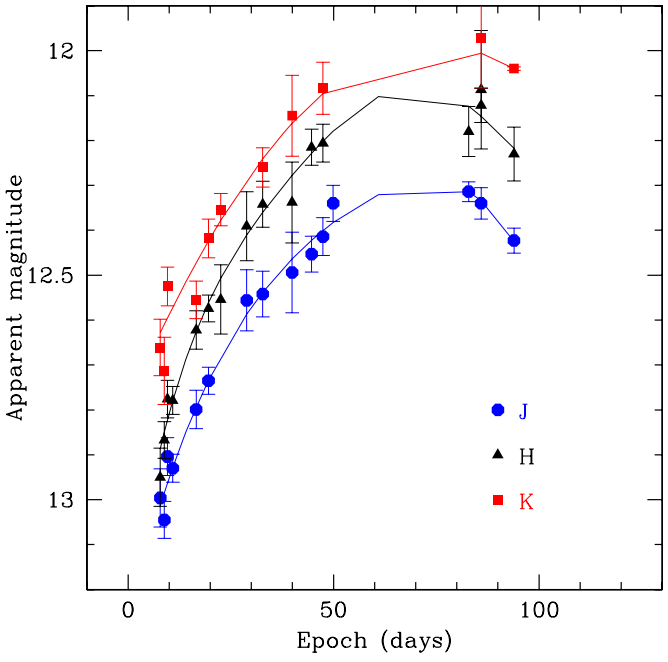

Figure 4. Photometric evolution in the *JHK* system.
(A color version of this figure is available in the online journal.)

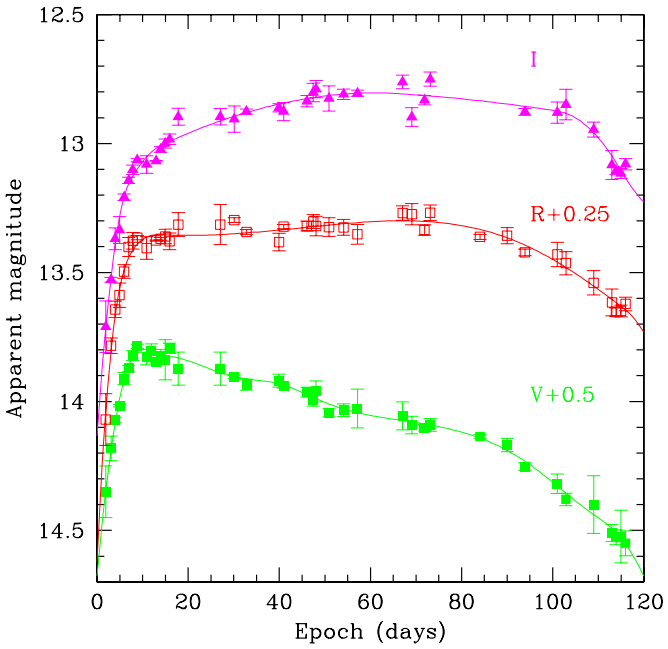

Figure 5. Photometric evolution in the *V*, *R*, and *I* bands, between day 1 and day 120. Data points are interpolated with cubic splines for visualization purposes.
(A color version of this figure is available in the online journal.)

with such behavior. Unfortunately, we do not have convincing evidence of the minima in the *V*, *R*, and *I* bands, claimed by Bose et al. (2013) at day 42, 39, and 31, respectively. Our *V*-band photometry shows quite a constant decline from day ∼25 to day ∼120, i.e., to the end of the plateau phase; the *R*-band light curve suggests a sharp rise to the plateau phase, which in this band lasts from day ∼10 to day 85; the *I*-band light curve also reveals a sharp rise up to day ∼10, followed by a slower rise to day ∼60 and a stable plateau that lasts up to day ∼100. Our Sloan *r*, *i*, and *z* light curves behave consistently. Interestingly, we observe a possible small flattening in the *I* band at day ∼10, followed by a quite steep rise between day ∼12 and day 17, also visible in the Sloan *r*, *i*, and *z* bands. Finally, the NIR *J*, *H*, *K* photometry shows a steady brightening up to day 64, with behavior similar to other Type IIP SNe (e.g., SN 2005cs, Pastorello et al. 2009). The apparent drop at day ∼95 could be an artifact, due the poor quality of the TCS data, where only one reference star was available.

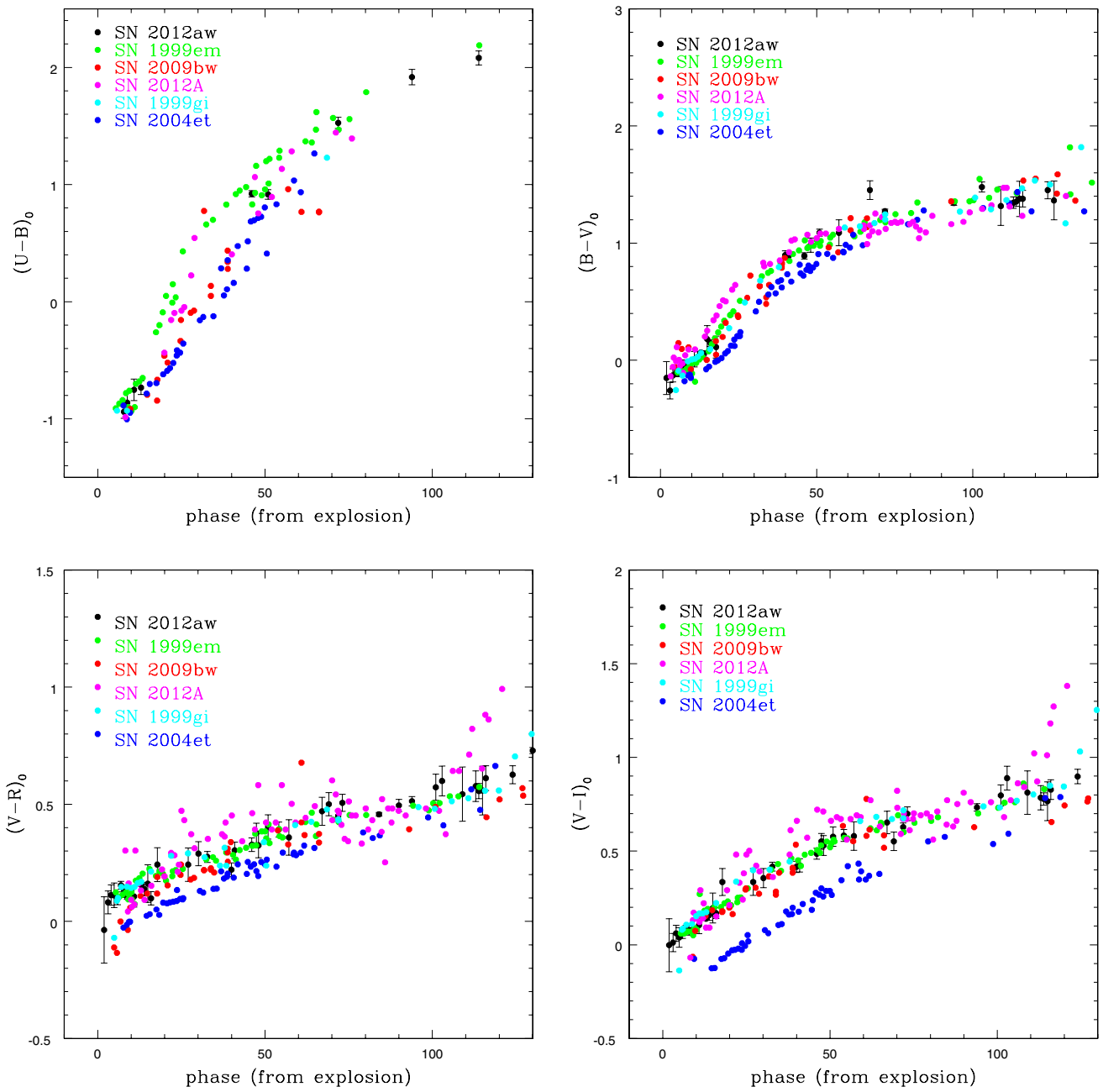

Figure 6. Dereddened color evolution of SN 2012aw in the *UBVRI* system, compared with other Type IIP SNe in the literature. The adopted extinction coefficients were taken from the papers quoted in the text.

(A color version of this figure is available in the online journal.)

Figure 6 shows the $U-B$, $B-V$, $V-R$, and $V-I$ color evolution of SN 2012aw during the photospheric phase, compared to those of other literature SNe. Colors of all SNe have been dereddened (see Section 3), for a proper comparison. The color evolution appears to be similar to that of other Type IIP SNe in the literature, namely SN 2012A (Tomasella et al. 2013), SN 1999em (Elmhamdi et al. 2003), SN 2009bw (Inserra et al. 2012), SN 1999gi (Leonard et al. 2002), and SN 2004et (Maguire et al. 2010). The plots show that SN 2012aw follows the typical evolution of Type IIP events, with a rapidly increasing $B-V$ color for the first 40 days, followed by a flattening of the curve.

Finally, Figure 7 depicts the time evolution of the intrinsic NIR coolers $J-H$ and $J-K$. For the sake of completeness, we also show the color curves of SN 1999em (Elmhamdi et al. 2003) and of SN 2004et (Maguire et al. 2010), for which we have a satisfactory time coverage in the NIR bands. Individual color curves show a rather large scatter, likely due to the photometric errors, but overall the three SNe show a similar behavior with a very small color evolution during the monitored period.

5. SPECTROSCOPY

5.1. Spectroscopic Observations and Data Reduction

Spectroscopic data were collected mostly during the first three months of evolution. We followed the spectroscopic evolution over 35 epochs from day 1 to day 94, in a wavelength range from 3300 to 25000 Å. Optical long-slit medium resolution

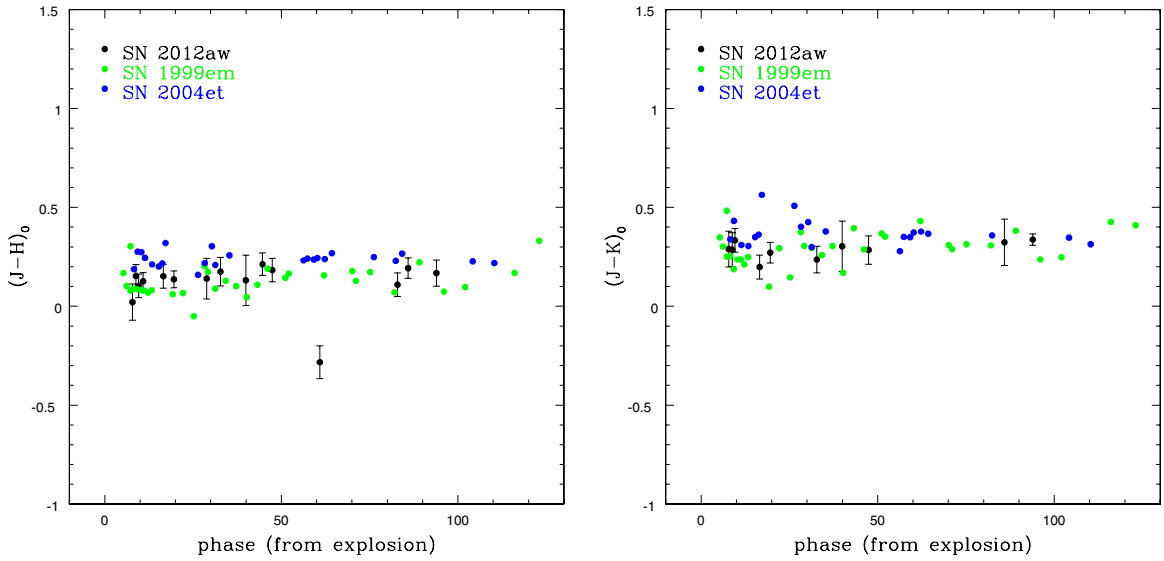

Figure 7. ($J - H$) and ($J - K$) color evolution of SN 2012aw, compared with SN 1999em and SN 2004et. Individual color curves have been dereddened according to the papers quoted in the text.

(A color version of this figure is available in the online journal.)

spectra were collected with the Boller & Chivens spectrograph at the Asiago 1.22 m telescope (3300–7800 Å, 12 epochs), ALFOSC at the NOT 2.56 m (3200–9100 Å, 5 epochs), AFOSC at the Ekar 1.82 m (3500–11000 Å, 4 epochs), DOLORES at the TNG 3.58 m (3000–10000 Å, 2 epochs), EFOSC2 at the NTT (3700–9300, 2 epochs), CAFOS at the CAHA 2.2m (3200–7000 Å, 1 epoch), and ISIS at the WHT (5400–9500 Å, 1 epoch). Near-infrared low resolution spectra were obtained with FIRE at the Magellan 6.5m telescope (8000–25000 Å, 4 epochs), and NICS at the TNG (9000–25000 Å, 1 epoch). High-resolution spectra were collected with SARG at the TNG (4600–7900 Å, 1 epoch, and 5000–10100 Å, 1 epoch), and with ISIS at the WHT (3500–5200 Å, 1 epoch). Table 5 lists all the spectroscopic observations, with the instruments and the instrumental setups.

FIRE (Folded-Port Infrared Echellette) spectra were reduced using a custom-developed IDL pipeline (Hsiao et al. 2013). All other spectra were pre-reduced in a standard fashion (overscan and bias subtraction, trimming, flat-fielding) by using the tools available in IRAF. Wavelength calibration was carried out taking spectra of arc lamps with the same instrumental setup used for the science observations. Calibrated spectra were corrected for the heliocentric recessional velocity of the host galaxy. Flux calibration was performed through a comparison with selected spectrophotometric standard stars, obtained during the same nights as the scientific observations and with the same instrumental setup. Finally, the absolute flux calibration of the spectra was verified by comparing the integrated flux in the *UBVRI* bands, measured using the IRAF package CALCPHOT, with the corresponding photometric measurements. When the spectra were collected on nights for which no photometry was available, a simple average of the adjacent photometric measurements was adopted. For spectra not bracketed by two consecutive photometric measurements, the polynomial light curve, discussed in the previous section, was used as a reference. Differences between the spectro-photometric and the photometric fluxes where corrected by multiplying and fitting the spectra with suitable coefficients. After the correction, the difference between the spectro-photometric and the photometric

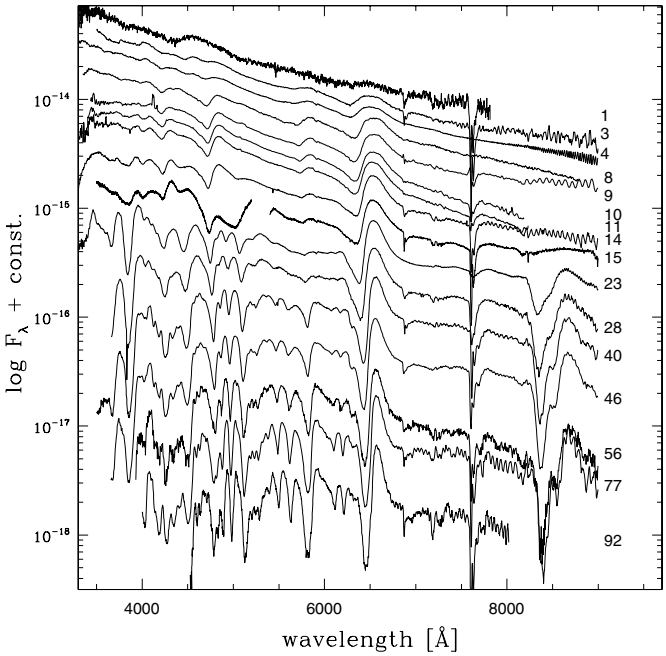

Figure 8. Spectral time evolution of SN 2012aw. Individual spectra are scaled in flux by an arbitrary quantity for clarity. Numbers on the left indicate the epoch from core-collapse.

magnitudes were between 0.01 and 0.05 mag. The same procedure was adopted for the NICS near-infrared spectra. It is worth noting that CALCPHOT adopts the Bessell & Brett (1988) NIR photometric system, while our photometry was calibrated onto the 2MASS system. We therefore transformed the CALCPHOT synthetic photometry into the 2MASS system following Carpenter (2001). Finally, we corrected the spectra for the adopted reddening.

5.2. Spectral Time Evolution

Figure 8 shows the optical spectral evolution of SN 2012aw, with the phases relative to the adopted explosion epoch, while

Table 5
Log of the Spectroscopic Observations

Date (dd/mm/yyyy)	JD 240000+	Epoch (days)	Range (Å)	Dispersion (Å mm^{-1})	Instrument
17/03/2012	56004.5	2.0	3300–7800	169	Asiago1.2m + BC
19/03/2012	56006.6	4.1	3300–7800	169	Asiago1.2m + BC
19/03/2012	56006.7	4.2	3200–9100	220	NOT + ALFOSC
20/03/2012	56007.6	5.1	3300–7800	169	Asiago1.2m +BC
20/03/2012	56007.8	5.3	3000–8400	187	TNG + LRS
20/03/2012	56007.8	5.3	4500–10000	193	TNG + LRS
21/03/2012	56008.6	6.1	3300–7800	169	Asiago1.2m + BC
21/03/2012	56008.8	6.3	4600–7900	61	TNG + SARG
22/03/2012	56009.6	7.1	3300–7800	169	Asiago1.2m + BC
23/03/2012	56010.7	8.2	3300–7800	169	Asiago1.2m + BC
24/03/2012	56011.8	9.3	3200–7000	185	CAHA2.2m + CAFOS
25/03/2012	56012.7	10.2	3300–7800	169	Asiago1.2m + BC
26/03/2012	56013.7	11.2	5000–11000	191	Ekar1.8m + AFOSC
26/03/2012	56013.8	11.3	3500–7700	292	Ekar1.8m + AFOSC
27/03/2012	56014.8	12.3	3500–7700	292	Ekar1.8m + AFOSC
28/03/2012	56015.8	13.3	3500–7700	292	Ekar1.8m + AFOSC
29/03/2012	56016.7	14.2	3300–7800	169	Asiago1.2m + BC
29/03/2012	56016.8	14.3	5000–10100	95	TNG + SARG
30/03/2012	56017.6	15.1	9000–14500	297	TNG + NICS
30/03/2012	56017.6	15.1	14000–25000	605	TNG + NICS
30/03/2012	56017.8	15.3	3200–9100	220	NOT + ALFOSC
31/03/2012	56018.4	15.9	3300–7800	169	Asiago1.2m + BC
31/03/2012	56018.6	16.1	3500–5200	64	WHT + ISIS
31/03/2012	56018.6	16.1	5400–9500	120	WHT + ISIS
02/04/2012	56020.3	17.8	3300–7800	169	Asiago1.2m + BC
08/04/2012	56025.4	22.9	3000–8400	187	TNG + LRS
08/04/2012	56025.4	22.9	4500–10000	193	TNG + LRS
08/04/2012	56025.5	25.0	8000–25000	446	Magellan + FIRE
11/04/2012	56028.6	26.1	8000–25000	446	Magellan + FIRE
13/04/2012	56030.4	27.9	3700–9300	185	NTT + EFOSC2
25/04/2012	56043.5	41.0	3200–9100	220	NOT + ALFOSC
30/04/2012	56047.6	45.1	8000–25000	446	Magellan + FIRE
01/05/2012	56048.9	46.4	3700–9300	185	NTT + EFOSC2
07/05/2012	56054.5	52.0	8000–25000	446	Magellan + FIRE
11/05/2012	56058.6	56.1	3200–9100	220	NOT + ALFOSC
01/06/2012	56080.4	77.9	3200–9100	220	NOT + ALFOSC
16/06/2012	56095.4	92.9	3300–7800	169	Asiago1.2m + BC

Notes. For each spectrum, we list the UT observation date, the JD, the epoch from the explosion, the wavelength range, the dispersion and the instrument.

a comprehensive atlas of the identified features is shown in Figure 9, at relevant phases. The first spectrum, taken less than two days after the estimated explosion, exhibits an almost featureless hot continuum. Interestingly enough, a "bump-shaped" feature is clearly visible at about 4600 Å. This bump fades very quickly, and it is no longer visible at the epoch of *V*-band maximum (day ∼ 9). A similar feature was also reported and discussed for SN 2009bw (Inserra et al. 2012). A possible identification is with a blend of highly ionized C and N features (also discussed for the Type IIn event SN 1998S, Fassia et al. 2001). The second spectrum, collected on day ∼3, shows the emergence of the typical H_α line, as well as the He I feature at ∼5876 Å. Initially, the H_α line shows a weak absorption component and a boxy emission. This feature may be the signature of a weak interaction with the circumstellar medium (see also SN 2007od, Inserra et al. 2011). This is also suggested by early radio observations (Stockdale et al. 2012; Yadav et al. 2012). The He I feature is no longer visible after day 15, while slightly blueward of He I a possible blend of the sodium doublet Na ID (5890, 5896 Å) with Ba II appears. This feature is visible as a small peak in the early spectra, but it clearly develops a P-Cygni profile by day 28. On day 8 we also observe a faint absorption structure at ∼5500 Å, which Bose et al. (2013) suggest to be a possible high-velocity component of He I. At the epoch of the *V*-band maximum (day ∼ 9), the H_α, H_β, H_γ, and H_δ lines are clearly visible. Typical Type IIP SNe metal lines are visible in the bluest part of the spectra after the *V*-band maximum, namely the Fe II, Ti II, Sc II, Ba II, and Ca II H and K features. As the ejecta expand (from day 24), the continuum becomes weaker and redder in the UV-blue part of the spectra, while other lines appear redward of 5000 Å. In particular, a strong Ca II P-Cygni feature stands out at ∼8570 Å on day 23, which at later epochs (see day 77) deblends into the three Ca II IR triplet components at 8498 Å, 8542 Å, and 8662 Å.

Figure 10 shows the NIR spectroscopic evolution. The first spectrum has been masked in the regions of low atmospheric transmission, since they appeared very noisy. Our time coverage ranges from day 15 to day 53. The H I Paschen series is clearly visible at all reported phases, with Pa_γ (10938 Å) possibly blended with He I (10830 Å). A possible blend of the Brackett Br_γ line with the Na I is also visible in all spectra. Redward of the Ca II NIR triplet an Fe II line is visible, which could be

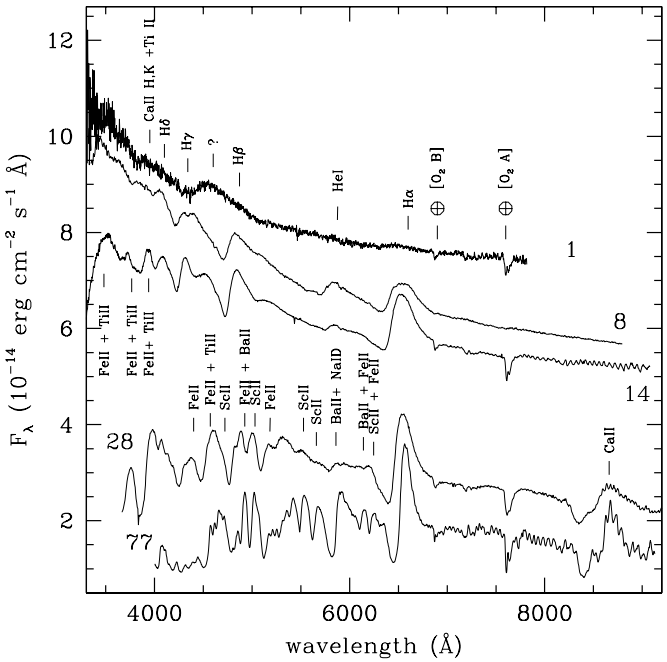

Figure 9. Line identification of the most prominent features of selected spectra of SN 2012aw. Individual spectra have been shifted in flux by an arbitrary quantity for clarity. Numbers on the two sides show the epochs from the explosion.

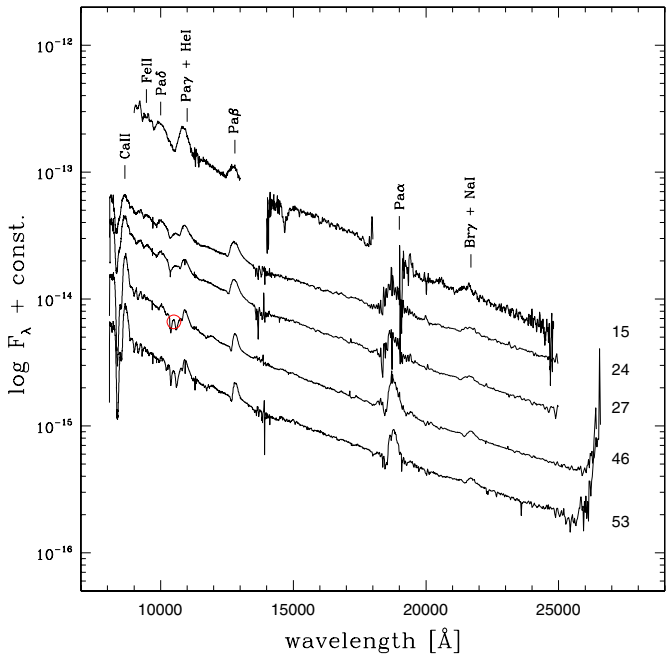

Figure 10. NIR spectra of SN 2012aw. Individual spectra have been shifted in flux for clarity. The most prominent features have been labeled. Numbers on the left indicate the epochs from the explosion. The red open circle marks the position of the unidentified feature discussed in the text.

blended with Paschen Pa_ϵ. Finally, we note the development of an unidentified P-Cygni line on day 24 at ∼10400 Å. Searching for a possible identification, we consulted the National Institute of Standards and Technology archive[23] and the SYNOW spectral synthesis code (e.g., Millard et al. 1999, Branch et al. 2002; Parrent et al. 2007 for the SYNOW 2.0 description), but could not find a reasonable match with usual ions showed by SNe.

[23] http://www.nist.gov/pml/data/asd.cfm

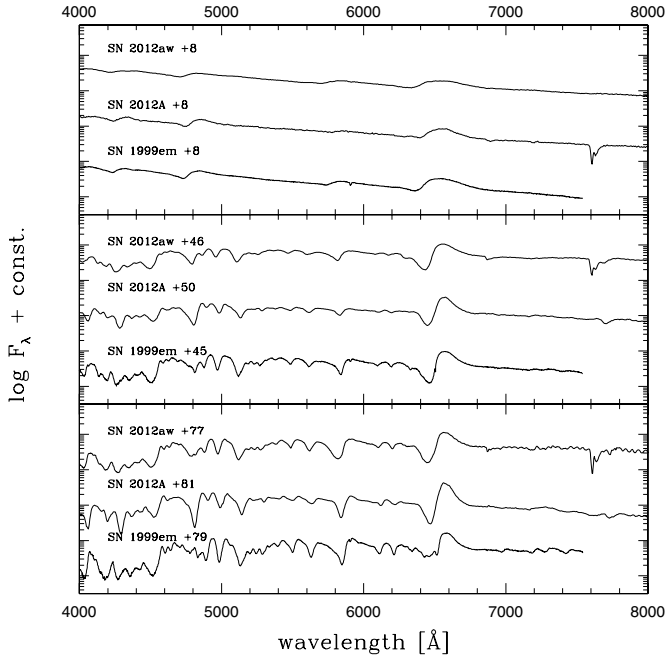

Figure 11. Comparison of the SN 2012aw spectra at selected phases with the Type IIP SNe SN199em and SN 2012A at similar phases. Top panel: about a week after explosion; middle panel: at middle plateau phase (∼50 days); bottom panel: in advanced plateau phase (∼80 days).

Therefore, we tentatively suggest that this is a high-velocity Pa_γ line. If this is the case, the Pa_γ absorption clearly splits into two components (10340 Å and 10560 Å) in the day 46 spectrum, which would correspond to velocities of ∼16000 and ∼10000 km s^{-1}, respectively. However, we do not see similar features for the other H lines.

In Figure 11 we compare the spectra of SN 2012aw at various phases (around maximum, at about the middle of the plateau phase, and at the advanced plateau phase), with those of other well-studied Type IIP SNe, namely SN 1999em (Elmhamdi et al. 2003) and SN 2012A (Tomasella et al. 2013). All the spectra were corrected to the rest wavelength and for the reddening. The spectra at all phases are very similar, with a blue continuum at early phases, the subsequent development of the typical Balmer lines, and the emergence of metal lines, at about one month.

6. PHYSICAL PARAMETERS

6.1. Bolometric Light Curve and ^{56}Ni Mass

A bolometric light curve (Figure 12) was obtained by integrating our photometric measurements and the *Swift* UV photometry (Bayless et al. 2013), and using the above adopted reddening and the distance modulus. We converted *uvw2 uvw1 UBVRIJHK* magnitudes[24] into monochromatic fluxes at the effective wavelength of the filter, then corrected these fluxes for the adopted extinction according to the extinction law from Cardelli et al. (1989), and finally integrated the resulting SED over the range of wavelength, after assuming zero flux at the integration limits. We estimated the flux only for the phases in which *V*-band observations were available. The photometric data in the other bands were estimated at these phases by interpolating magnitudes in adjacent nights. Finally, flux was converted into luminosity using the adopted distance modulus. The peak of the

[24] We did not use the *Swift* uvm2 band due to the lower number of measurements available and to the higher photometric errors in this band.

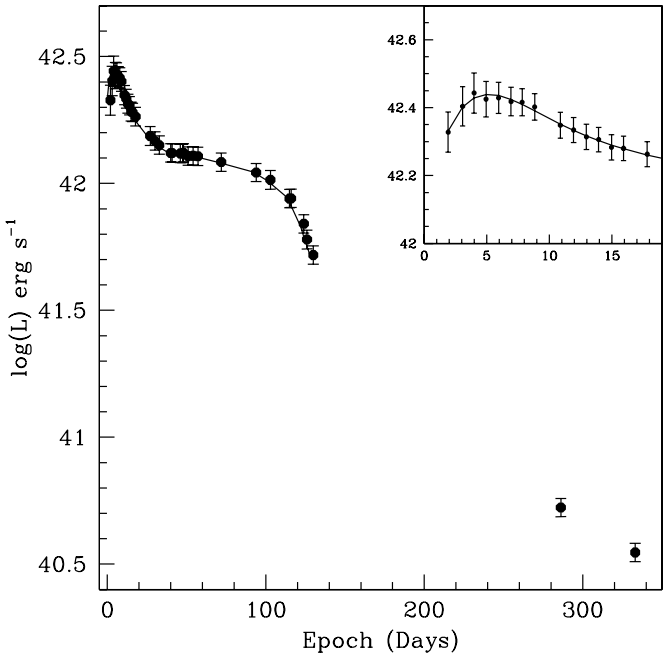

Figure 12. *uvoir* bolometric light curve of SN 2012aw. The bolometric luminosity was obtained from a full set of *Swift* $uvw2$, $uvw1$, Johnson–Cousins *UBVRI*, and near-infrared *JHK* measurements, following the procedure described in the text. Error bars are generally negligible with respect to the size of the plotted points. The inset shows a zoom of the first 20 days.

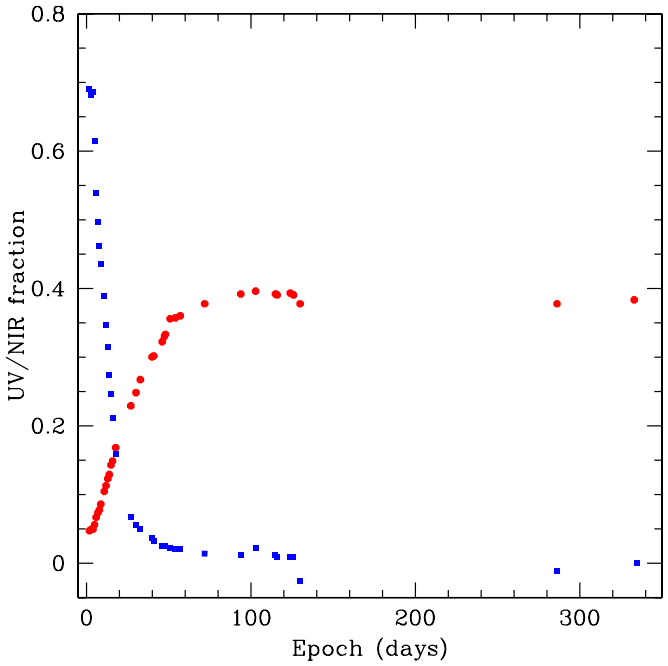

Figure 13. UV (blue filled squares) and NIR (red filled circles) contribution to the total flux.

(A color version of this figure is available in the online journal.)

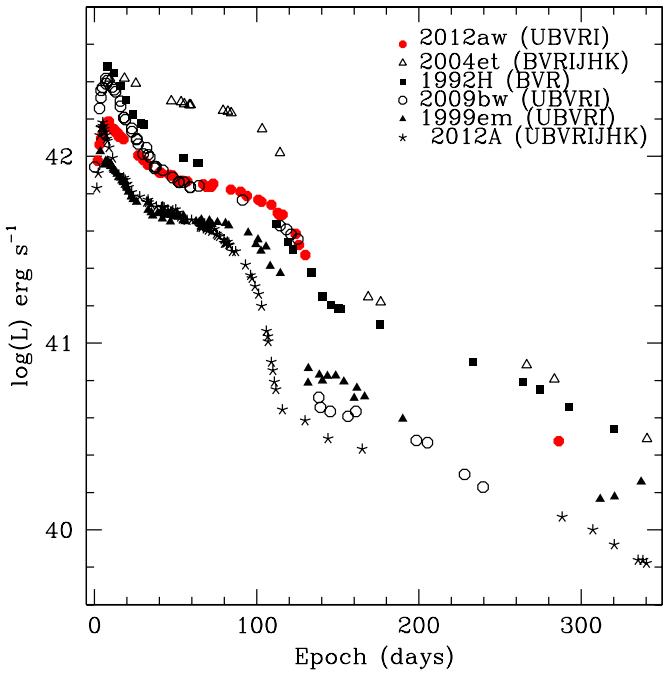

Figure 14. *UBVRI* Pseudo-bolometric light curve of SN 2012aw. The light curve is compared with the Type IIP SNe SN 1992H, SN 1999em, SN 2004et, SN 2009bw, and SN 2012A.

(A color version of this figure is available in the online journal.)

bolometric luminosity is reached at day ∼4 at a luminosity of $L_{\rm bol} = (2.8 \pm 0.5) \times 10^{42}$ erg s^{-1}. In Figure 12 we also show a close-up of the evolution of the bolometric luminosity during the first 20 days. The maximum is quite sharply reached, followed by a decline with a sort of flattening, and by a change in the decline slope at day ∼9. The latter coincides with the already discussed feature in the *I* band (see Section 4.2).

Taking advantage of our full UV-optical-NIR (*uvoir*) data set, in Figure 13 we show the contribution of the *Swift* $uvw2$, $uvw1$ bands (filled squares) and of the NIR bands (filled circles) to the total flux. The NIR contribution shows a progressive rise during the photospheric phase up to the end of the plateau, and then remains approximately constant during the nebular phase, at least until day ∼330. This behavior is similar to other Type IIP SNe, such as SN 2004et (Maguire et al. 2010) and SN 2007od (Inserra et al. 2011). The UV contribution steeply decreases after the explosion, showing a "knee" at the beginning of the plateau. By the middle of the plateau, it decreases to the 2% level of the total flux at the middle of the plateau, and becomes negligible ($\lesssim$1%) at the end of the photospheric phase. In order to compare SN 2012aw with other SNe found in the literature, for which only a limited wavelength coverage was available, we also calculated a *UBVRI* pseudo-bolometric light curve of SN 2012aw. The comparison of SN 2012aw with SN 1992H (Clocchiatti et al. 1996), SN 1999em (Elmhamdi et al. 2003), SN 2009bw (Inserra et al. 2012), SN 2004et (Maguire et al. 2010), and SN 2012A (Tomasella et al. 2013) in Figure 14 shows that SN 2012aw belongs to the bright branch of the luminosity distribution of Type IIP events. The ^{56}Ni mass was estimated by comparing the luminosity of SN 2012aw with that of SN 1987A during the nebular phase, assuming a similar $\gamma-$ray deposition fraction such that:

$$M\left(^{56\rm Ni}_{12\rm aw}\right) = M\left(^{56\rm Ni}_{87\rm A}\right) \times \frac{L_{12\rm aw}}{L_{87\rm A}}\, M_{\odot} \qquad (3)$$

where the luminosities must be compared at similar epochs. We adopted for SN 1987A a ^{56}Ni mass of $M(^{56\rm Ni}_{87\rm A}) = 0.073 \pm 0.012\, M_{\odot}$, which is the weighted mean of the values given by Arnett & Fu (1989) and by Bouchet et al. (1991), and the ultraviolet-optical-infrared bolometric luminosity given by Bouchet et al. (1991). We therefore obtained $M(^{56\rm Ni}_{12aw}) = 0.056 \pm 0.013\, M_{\odot}$, as an average of the individual estimates at days 286 and 333. This value is in agreement, within the uncertainties, with the estimate of $0.06 \pm 0.01\, M_{\odot}$ given by

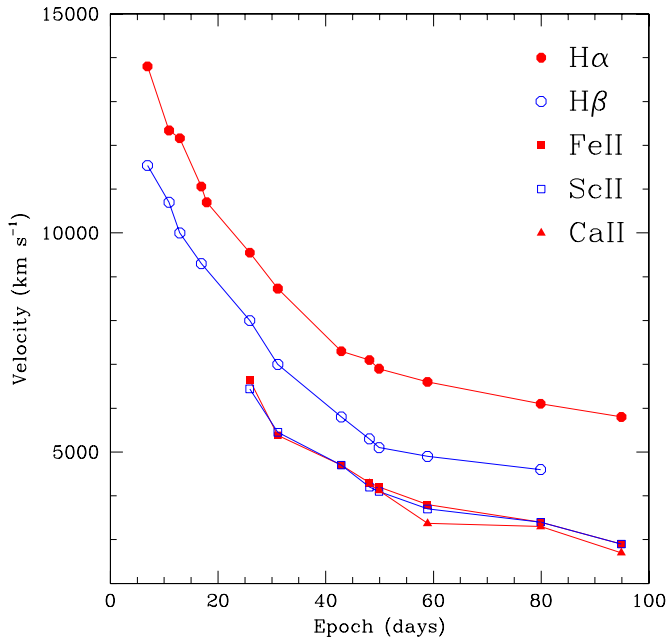

Figure 15. Line velocity evolution, estimated from the Doppler shift of the absorption minima, of Hα, Hβ, Fe II (5169), Sc II (6256), and Ca II (8520).
(A color version of this figure is available in the online journal.)

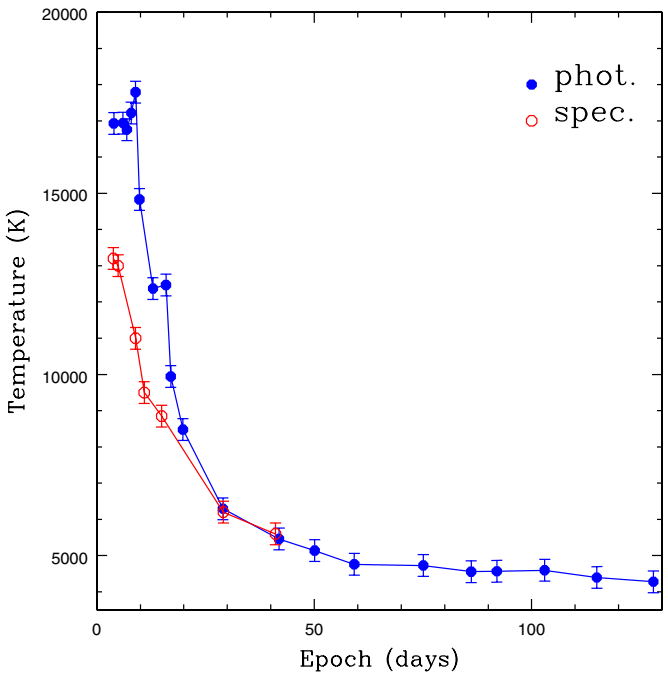

Figure 16. Temperature evolution of SN 2012aw, derived from blackbody fits to the observed fluxes in the range from the *Swift* $uvw2$- to the *K*-bands (blue filled circles) and from the continuum of selected spectra (red open circles).
(A color version of this figure is available in the online journal.)

Bose et al. (2013), obtained with the same method, and with the 0.062 $M_{\odot}$, estimate of Jerkstrand et al. (2014), based on the spectral synthesis models of the nebular phase.

The estimated nickel mass can be compared with the values inferred for our SN sample, which range from ∼0.02 $M_{\odot}$ (SN 1999em, Elmhamdi et al. 2003; SN 2009bw, Inserra et al. 2012) to ∼0.06 $M_{\odot}$ (SN 2004et, Maguire et al. 2010) and ∼0.07 $M_{\odot}$ (SN 1992H, Clocchiatti et al. 1996). These estimates, adopted from the original papers, were derived using the same method as we follow for SN 2012aw, except for SN 1992H, whose ^{56}Ni mass was estimated from a theoretical light curve.

6.2. Expansion Velocity, Blackbody Temperature, and SED Evolution

Figure 15 shows the evolution of the photospheric expansion velocities measured from the Doppler-shift of absorption minima of the Hα, Hβ Fe II (5169 Å), Sc II (6245 Å), and Ca II (8520 Å) lines. Measurements have been performed by fitting the lines with a single Gaussian profile. The Hα and Hβ lines are characterized by the highest velocities, starting from ∼14000 and ∼12000 km s^{-1} on day 15, respectively. Their velocities rapidly decrease and, at about 50 days from the explosion, they reach an almost constant value of ∼7000 and ∼5000 km s^{-1}, respectively. We note that these values appear larger than in other Type IIP SNe at similar phases, (e.g., SN 2012A, Tomasella et al. 2013, their Figures 12 and 13; SN 2009bw, Inserra et al. 2012, their Table 9; SN 2004et, Maguire et al. 2010, their Figure 20). As is typical in Type IIP SNe, Hα and Hβ velocities are higher, since these spectral features are formed at larger radii than those of most metal lines. The Fe II and Sc II velocities are considered to be better tracers of the photospheric velocity, since the relevant transitions have small optical depths. They show behavior very similar to each other, both settling to ∼3000 km s^{-1} after about two months. Other luminous Type IIP SNe such as SN 2009bw (Inserra et al. 2012), SN 2004et (Maguire et al. 2010), and SN 1999em (Elmhamdi et al. 2003) exhibit similar line velocities, while those of SN 2005cs appear lower (see Maguire et al. 2010, their Figure 21). The velocity evolution of the Ca II feature resembles that of the Fe II and Sc II lines, but with a slightly larger scatter, due to measurement uncertainties.

Figure 16 shows the time evolution of the photospheric temperature, evaluated with a blackbody fit to the photometric data (blue filled circles) and to the spectral continuum (red open circles). In the first ∼20 days, photometry-based temperatures appear systematically hotter than the spectral-based measurements, while on day 25, the measurements agree within the uncertainties. A possible explanation of this behavior is that our spectra do not include the ultra-violet wavelengths covered by the *Swift* photometry. The evolution of the spectral continuum temperature looks similar to that in other Type IIP SNe (e.g., Inserra et al. 2012, their Figure 11). Interestingly, between day ∼12 and day ∼16 a small plateau in the temperature evolution is visible. The same feature is also visible in Bose et al. (2013), their Figure 7, and it is also suggested in our individual light curves, already discussed. This is in correspondence with the light curve plateau transition (see Figure 5). Finally, we note that Figure 16 shows an almost constant temperature from day ∼30, in agreement with the Bayless et al. (2013) findings for SN 2012aw.

Figure 17 shows the SED evolution between day ∼4 and day ∼132. Our SED was based on our optical-NIR photometry, complemented with *Swift* UV $uvw2$ and $uvw1$ data (Bayless et al. 2013) which cover approximately the first 60 days after the explosion. The wavelength coverage ranges between ∼2000 Å to ∼22000 Å. Superimposed to the points are, for each epoch, blackbody continuum fits. During this time, the optical-NIR fluxes in the range ∼4000–22000 Å well resembles single blackbody curves.

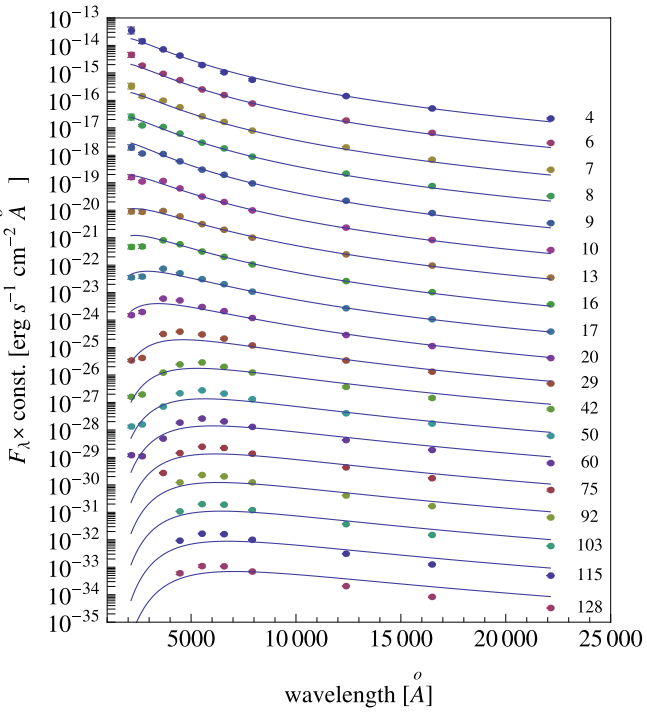

Figure 17. Time evolution of the spectral energy distribution of SN 2012aw. Filled circles depict the fluxes at the effective wavelengths of the photometric filters. Solid lines show the blackbody continuum fits. Numbers indicate the phases from core-collapse. Observed fluxes have been corrected for the adopted extinction and distance.

(A color version of this figure is available in the online journal.)

7. EXPLOSION AND PROGENITOR PARAMETERS

Some observational quantities, namely the bolometric luminosity, the length of the plateau, and the evolution of line velocities and continuum temperature at the photosphere can be used to constrain the relevant physical parameters of the SN, that is the ejected mass, the progenitor radius, the explosion energy and the amount of ^{56}Ni (e.g., Litvinova & Nadezhin 1985; Zampieri et al. 2003; Kasen & Woosley 2009).

We estimate these physical parameters for SN 2012aw by performing a simultaneous χ^2 fit of the aforementioned observational quantities against model calculations, using the same well-tested procedure adopted for modeling other core-collapse SNe (CC-SNe; e.g., SNe 2007od, 2009bw, 2009E, and 2012A; see Inserra et al. 2011; Inserra et al. 2012; Pastorello et al. 2012; Tomasella et al. 2013).

Two codes have been used to calculate the models: the semi-analytic code described in Zampieri et al. (2003) and the radiation-hydrodynamics code described in Pumo et al. (2010) and Pumo & Zampieri (2011). The first one solves the energy balance equation for a spherically symmetric, homologously expanding envelope with constant density. It is used to perform preparatory studies aimed at narrowing down the parameter space describing the CC-SN progenitor at the explosion and, consequently, to guide the more realistic but time-consuming simulations performed with the radiation-hydrodynamics code. This code is able to simulate the evolution of the physical properties of the CC-SN ejecta and the evolution of the main CC-SN observables up to the nebular stage, solving the equations of relativistic radiation hydrodynamics for a self-gravitating fluid which interacts with radiation. The main features of this code are as follows. (1) A fully implicit Lagrangian approach to the solution of the system of relativistic radiation hydrodynamics equations. (2) An accurate treatment of radiative transfer coupled with relativistic hydrodynamics. (3) a self-consistent treatment of the evolution of ejected material taking into account both the gravitational effects of the compact remnant and the heating effects due to decays of radioactive isotopes synthesized during the CC-SN explosion.

We point out that our modeling using both the aforementioned codes is appropriate only if the emission from the CC-SN is dominated by the thermal balance in the expanding ejecta. In the case of SN 2012aw, there could be contamination from an early interaction with circumstellar matter (see Section 1), which may partially affect the observables during the early post-explosion evolution (first ∼30 days after explosion). Nevertheless, since there is no evidence that such contamination continues and dominates during most of the evolution, we assume that our modeling can be applied to SN 2012aw and returns a robust estimate of the physical properties of the progenitor (as already done for other CC-SNe with possible contamination from a relatively "weak" interaction like SNe 2007od and 2009bw; see Inserra et al. 2011, 2012). However, in the χ^2 fit we do not include the data taken at early phases because the behavior of the observational quantities could be contaminated by a possible interaction. In addition, during such phases there is significant emission from the outermost shell of the ejecta, which is accelerated to very high velocities and is not in homologous expansion (Pumo & Zampieri 2011). The structure, evolution, and emission properties of this shell are not well reproduced in our simulations because at present we adopt an *ad hoc* initial density profile, not one consistently derived from a post-explosion calculation.

The explosion epoch and distance modulus adopted here are those reported in Section 1 and Section 2, respectively. A ^{56}Ni mass of ∼0.06 $M_\odot$ is assumed (see Section 6.1).

We computed an extended grid of semi-analytical models, covering a significant range in mass. In Figure 18 we show the χ^2 of the models as a function of the ejected mass. The distribution has a broad structured minimum extending from ∼15 to ∼28 $M_\odot$. Significant local minima occur at ∼16 $M_\odot$, ∼19 $M_\odot$, and ∼25 $M_\odot$, while an additional less prominent minimum occurs at ∼12 $M_\odot$. We explored the minima at ∼19 and ∼25 $M_\odot$ to constrain the parameter space for the radiation-hydrodynamics simulations. The latter were run varying the ejected mass in the range 16–27 $M_\odot$ and are in fair agreement with the semi-analytical models. Figure 19 shows the result for the best fitting semi-analytical and hydrodynamical simulations, giving an ejected mass of ∼20 $M_\odot$, a total (kinetic plus thermal) energy of 1.5 foe and an initial radius of 3×10^{13} cm. These values are consistent with a scenario where the SN is produced by a relatively standard explosion of a supergiant progenitor with a total mass of ∼21 $M_\odot$ at explosion. We note that the local minimum of the χ^2 at ∼16 $M_\odot$ is close to the ∼15 $M_\odot$ estimate of the progenitor mass given by Kochanek et al. (2012) and Bose et al. (2013), and to the 17–18 $M_\odot$ value given by Van Dyk et al. (2012). However, with an ejected mass of ∼15 $M_\odot$, our radiation-hydrodynamics code fails to reproduce all the observed features. In particular, it is not possible to reproduce at the same time the observed expansion velocity and the length of the plateau, which are diagnostics that are basically independent of the adopted reddening and distance. As a matter of fact, when adopting the high reddening estimate $E(B-V) = 0.19$ mag discussed above, the same procedure gives an ejected mass of ∼21–23 $M_\odot$, a total energy of 1.6–1.7 foe, and initial radius of 2–4 $\times$ 10^{13} cm.

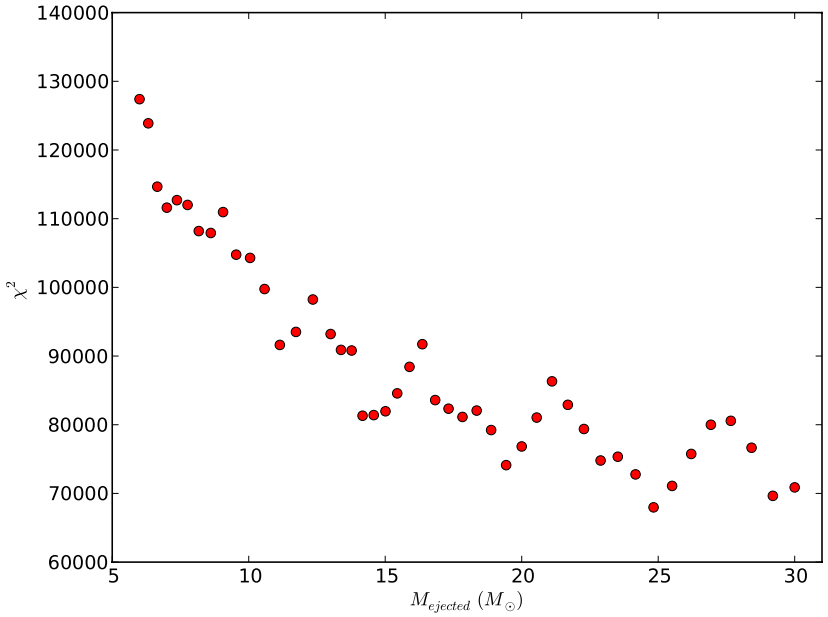

Figure 18. χ^2 distribution of the fit of the semi-analytical model to the observed quantities, as a function of the estimated ejected mass.
(A color version of this figure is available in the online journal.)

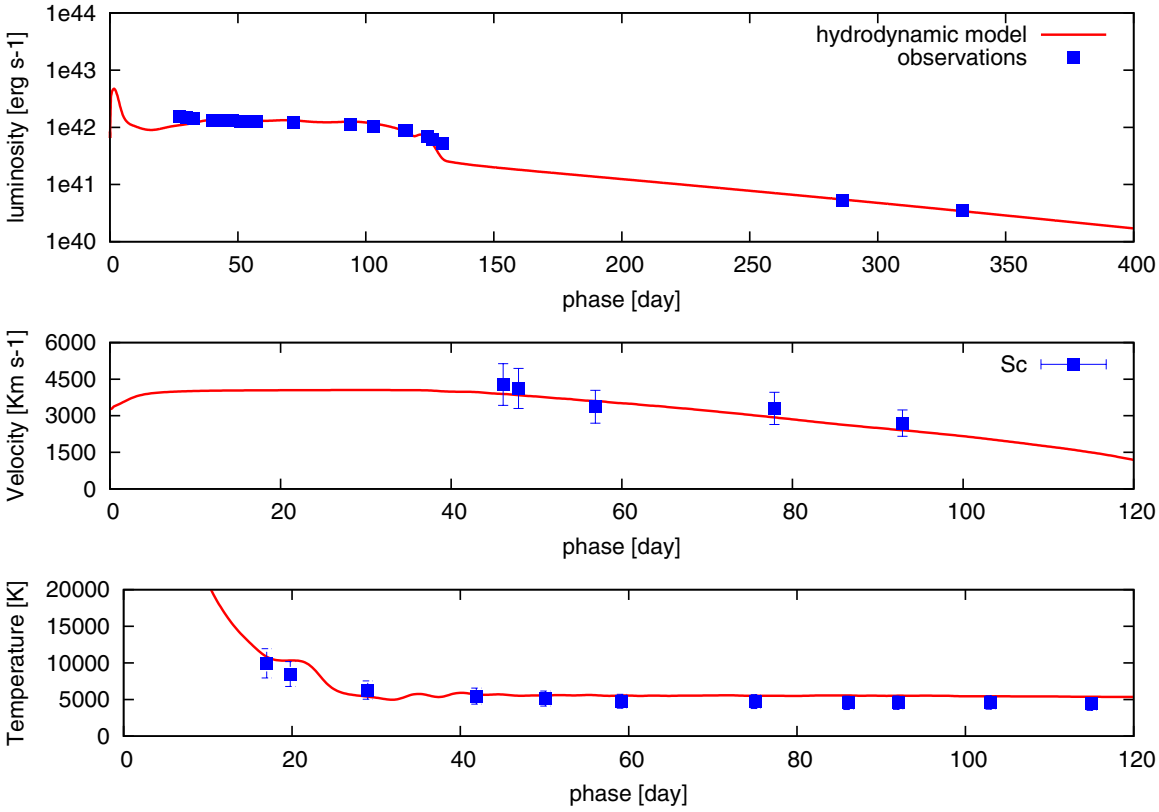

Figure 19. Comparisons of the evolution of the main observables of SN 2012aw with the best-fit model computed with our radiation-hydrodynamics code (total energy 1.5 foe, initial radius 3×10^{13} cm, envelope mass 19.6 $M_\odot$). Top, middle, and bottom panels show the bolometric light curve, the photospheric velocity, and the photospheric temperature as a function of time. To better estimate the photosphere velocity from observations, we use the minima of the profile of the Sc II lines.
(A color version of this figure is available in the online journal.)

8. DISCUSSION AND CONCLUSIONS

We have presented the results of our photometric and spectroscopic campaign of the Type IIP SN 2012aw. Our photometry maps the SN from the explosion up to the end of the plateau (at day $\sim$ 125), in the UV-optical-NIR bands. Moreover, two additional epochs were collected in the nebular phase (at day 286 and day 333), to get an estimate of the ^{56}Ni mass. Spectroscopic data map the SN evolution from day 2 to day 90. Our data allowed us to draw a detailed picture of SN 2012aw, by deriving all the relevant diagnostics, namely the expansion velocity and photospheric temperature

evolution, and estimating its physical parameters. We adopt the distance modulus ($\mu = 29.96 \pm 0.04$ mag) by averaging the Cepheids (Freedman et al. 2001) and the TRGB (Rizzi et al. 2007) distances, while estimating the Galactic reddening from Schlegel et al. (1998). The host reddening was evaluated by measuring the EW(Na ID) on a high-resolution spectrum, and adopting the Poznanski et al. (2012) calibration we derived $E(B-V) = 0.058 \pm 0.016$ mag. Taking into account a foreground reddening of $E(B-V) = 0.028$ mag, estimated from the Schlegel et al. (1998) maps, we end up with the total reddening (foreground and host) $E(B-V) = 0.086 \pm 0.02$ mag.

With the adopted distance and reddening values, our analysis of the bolometric light curve shows that SN 2012aw belongs to the high branch of Type IIP SNe luminosities and allows us to estimate an ejected ^{56}Ni mass of $\sim 0.056 \pm 0.013\ M_{\odot}$. The SED shows a generally good fit with a single blackbody curve.

From the collected spectra, we measure a fairly large initial expansion velocity of $\sim$14,000 km s^{-1} in the Hα line. After $\sim$50 days from the explosion, the Hα and Hβ lines settle on a constant value of $\sim$6000 and $\sim$5000 km s^{-1}, respectively. Starting from day $\sim$25, we obtain an expansion velocity of $\sim$3000 km s^{-1} from the Fe II and Sc II lines, which are known to be better tracers of the photospheric velocities. This behavior is in agreement with those shown by other luminous Type IIP SN, such as SN 2009bw (Inserra et al. 2012).

We estimate the physical parameters of SN 2012aw and its progenitor by means of the hydrodynamical modeling described in Section 7, which uses the radiation-hydrodynamics code (Pumo et al. 2010; Pumo & Zampieri 2011). Our simulations suggest that the envelope mass is $M_{\rm env} \sim 20\ M_{\odot}$, the radius is $R \sim 3 \times 10^{13}$ cm, the energy is $E \sim 1.5$ foe, and the initial ^{56}Ni in the $\sim$0.05–0.06 $M_{\odot}$ range. We explicitly note that our progenitor mass and radius estimates are in fair agreement with the independent evolutionary model-based values of Fraser et al. (2012a) based on a direct progenitor detection: $M_{\rm ZAMS} \sim$ 14–26 $M_{\odot}$ and $R > 500\ R_{\odot} \simeq 3.5 \times 10^{13}$ cm. Taken at face value, these estimates indicate a massive SN progenitor, with a mass significantly higher than the observational limit of $16.5 \pm 1.5\ M_{\odot}$ that raised the "RSG problem" (Smartt et al. 2009), thus is in good agreement with the higher mass limit of $21^{+2}_{-1}\ M_{\odot}$ found by Walmswell & Eldridge (2012). However, our values are considerably larger than those estimated by Kochanek et al. (2012), $L < 10^4\ L_{\odot}$, $M < 15\ M_{\odot}$, obtained by carefully modeling the circumstellar extinction and not simply assuming an interstellar extinction law for the circumstellar dust. Moreover, it has been reported in the literature that the ejecta masses estimated from the modeling are generally too high to be consistent with the initial masses determined from direct observations of SN progenitors (e.g., Utrobin & Chugai 2009, Maguire et al. 2010). However, the code used here gives lower ejecta masses, as also noted in Jerkstrand et al. (2012). It is interesting to compare our results with those obtained by Bose et al. (2013), who give an estimate of the explosion energy and the progenitor mass by using the analytical relations given by Litvinova & Nadezhin (1985) and adopting the radiation hydrodynamical simulations provided by Dessart et al. (2010). Their analysis points toward an explosion energy in the range 1–2 foe and a progenitor mass in the 14–15 $M_{\odot}$ range. It should be noted that Bose et al. (2013) found several similarities between SN 2012aw and SN 2004et and SN 1999em, on the basis of Utrobin & Chugai (2009) and Utrobin & Chugai (2011) investigations. However, in the same papers the estimated progenitor masses are quite large, of the order of 20–25 $M_{\odot}$. Moreover, Bose et al. (2013) found some evidence of interaction with the circumstellar medium, which could imply a large mass loss during the progenitor star's lifetime too large to be reconciled with a star of initial mass of 14–15 $M_{\odot}$. Clearly, such differences are due mostly to the different models adopted and to the fact that there is still an issue regarding reconciling progenitor masses (which are model dependent) with ejecta masses (also model dependent). Therefore, it would be interesting to perform a detailed comparison of the different available codes on the same objects, to check how consistent the results are.[25] It should also be noted that the analysis of the nucleosynthesis products of SN 2012aw performed by Jerkstrand et al. (2014) seems to rule out a high-mass progenitor, in that the observed lines consistent with a progenitor in the 14–18 $M_{\odot}$ range. However, as pointed out by the same authors, the link between progenitor mass and nucleosynthesis depends on some as yet uncertain processes in the input physics of the stellar evolution models, such as semi-convection, overshooting, and rotation. Quoting Jerkstrand et al. (2014, p. 3701): "Understanding the differences in results between progenitor imaging, hydrodynamical modeling, and nebular phase spectral analysis is a high priority in the Type IIP research field." Moreover, it is worth noting that, on the basis of our simulations, possible uncertainties in the local reddening do not have a dramatic impact on the estimate of the physical parameters of SN 2012aw. Indeed, when adopting the high reddening $E(B-V) = 0.19$ mag, our simulations give only slightly different values of the ejected mass, initial radius, and explosion energy.

Finally, it should be noted that, as stated by Brown & Woosley (2013, p. 7): "the best we can say at the present time is what supernova mass limits might be consistent with observations. The idea of a limiting mass is itself an approximation, since the compactness of the core is not a monotonic function of main sequence mass [...], especially in the interesting range 20–35 $M_{\odot}$."

We warmly thank our referee for helpful comments, which significantly improved the content and the readability of our manuscript.

This paper is based on observations collected at: the Copernico 1.82 m Telescope and Schmidt 67/92 Telescope operated by the INAF-Osservatorio Astronomico di Padova at Asiago, Italy, the Galileo 1.22 m Telescope operated by the Department of Physics and Astronomy of the University of Padova at Asiago, the 3.58 m Italian Telescopio Nazionale Galileo (TNG) operated on the island of La Palma by the Fundación Galileo Galilei of INAF (Istituto Nazionale di Astrofisica), and the CNTAC, proposal CN2012A-103. Data provided by the Rapid Eye Mount (REM) NIR camera (REMIR) under the program AOT25041.

We acknowledge the TriGrid VL project and the INAF-Astronomical Observatory of Padua for the use of computer facilities. M.L.P. acknowledges the financial support from the PRIN-INAF 2009 "Supernovae Variety and Nucleosynthesis Yields" (P.I.: S. Benetti) and PRIN-INAF 2011 "Transient Universe: from ESO Large to PESSTO" (P.I.: S. Benetti). F.B. acknowledges support from FONDECYT through Postdoctoral grant 3120227.

[25] A similar experiment was already performed to test how different evolutionary models could determine the star formation histories of resolved stellar populations (the *Coimbra Experiment*, see Skillman & Gallart 2002).

M.T.B., L.T., M.D.V., E.C., S.B., A.H., and A.P. are partially supported by the PRIN-INAF 2011 with the project "Transient Universe: from ESO Large to PESSTO."

G.P. and F.B. acknowledge support from the "Millennium Center for Supernova Science" (P10-064-F), with input from the "Fondo de Innovacin para la Competitividad del Ministerio de Economia, Fomento y Turismo de Chile."

G.P. acknowledges partial support by "Proyecto interno UNAB DI-303-13/R."

N.E.R. and A.M.G acknowledge financial support by the MICINN grant AYA2011-24704/ESP, and by the ESF EUROCORES Program EuroGENESIS (MINECO grants EUI2009-04170).

S.T. acknowledges support by the Transregional Collaborative Research Centre TRR 33 "The Dark Universe" of the German Research Foundation.

The research leading to these results has received funding from the European research Council under the European Union's Seventh Framework Programme (FP7/2007-2013)/ERC grant agreement No. 291222 (P.I.: S. J. Smartt).

REFERENCES

Ahn, C. P., Alexandroff, R., Allende Prieto, C., et al. 2012, ApJS, 203, 21
Arnett, W. D., Bahcall, J. N., Kirshner, R. P., & Woosley, S. E. 1989, ARA&A, 27, 629
Arnett, W. D., & Fu, A. 1989, ApJ, 340, 396
Barbon, R., Ciatti, F., & Rosino, L. 1979, A&A, 72, 287
Bayless, A. J., Pritchard, T. A., Roming, P. W. A., et al. 2013, ApJL, 764, L13
Beifiori, A., Sarzi, M., Corsini, E. M., et al. 2009, ApJ, 692, 856
Bessell, M. S., & Brett, J. M. 1988, PASP, 100, 1134
Bohlin, R. C., Savage, B. D., & Drake, J. F. 1978, ApJ, 224, 132
Bose, S., Kumar, B., Sutaria, F., et al. 2013, MNRAS, 433, 1871
Botticella, M. T., Smartt, S. J., Kennicutt, R. C., et al. 2012, A&A, 537, A132
Bouchet, P., Danziger, I. J., & Lucy, L. B. 1991, AJ, 102, 1135
Branch, D., Benetti, S., Kasen, D., et al. 2002, ApJ, 566, 1005
Brown, J. M., & Woosley, S. E. 2013, ApJ, 769, 99
Cappellaro, E., Evans, R., & Turatto, M. 1999, A&A, 351, 459
Cardelli, J. A., Clayton, G. C., & Mathis, J. S. 1989, ApJ, 345, 245
Carpenter, J. M. 2001, AJ, 121, 2851
Ciardullo, R., Feldmeier, J. J., Jacoby, G. H., et al. 2002, ApJ, 577, 31
Clocchiatti, A., Benetti, S., Wheeler, J. C., et al. 1996, AJ, 111, 1286
Coppola, G., Dall'Ora, M., Ripepi, V., et al. 2011, MNRAS, 416, 1056
Dahlen, T., Strolger, L.-G., Riess, A. G., et al. 2012, ApJ, 757, 70
Dessart, L., Livne, E., & Waldman, R. 2010, MNRAS, 408, 827
Ekström, S., Georgy, C., Eggenberger, P., et al. 2012, A&A, 537, A146
Elias-Rosa, N., Van Dyk, S. D., Cuillandre, J.-C., Cenko, S. B., & Filippenko, A. V. 2012, ATel, 3991, 1
Elmhamdi, A., Danziger, I. J., Chugai, N., et al. 2003, MNRAS, 338, 939
Fagotti, P., Dimai, A., Quadri, U., et al. 2012, CBET, 3054, 1
Fassia, A., Meikle, W. P. S., Chugai, N., et al. 2001, MNRAS, 325, 907
Ferlet, R., Vidal-Madjar, A., & Gry, C. 1985, ApJ, 298, 838
Filippenko, A. V. 1997, ARA&A, 35, 309
Fraser, M., Ergon, M., Eldridge, J. J., et al. 2011, MNRAS, 417, 1417
Fraser, M., Maund, J. R., Smartt, S. J., et al. 2012a, ApJL, 759, L13
Fraser, M., Maund, J. R., Smartt, S. J., et al. 2012b, ATel, 3994, 1
Freedman, W. L., Madore, B. F., Gibson, B. K., et al. 2001, ApJ, 553, 47
Gurovich, S., Freeman, K., Jerjen, H., Staveley-Smith, L., & Puerari, I. 2010, AJ, 140, 663
Hägele, G. F., Díaz, Á. I., Cardaci, M. V., Terlevich, E., & Terlevich, R. 2007, MNRAS, 378, 163
Hamuy, M., & Pinto, P. A. 2002, ApJL, 566, L63
Harutyunyan, A. H., Pfahler, P., Pastorello, A., et al. 2008, A&A, 488, 383
Henden, A., Krajci, T., & Munari, U. 2012, IBVS, 6024, 1
Hsiao, E. Y., Marion, G. H., Phillips, M. M., et al. 2013, ApJ, 766, 72
Immler, S., & Brown, P. J. 2012, ATel, 3995, 1
Inserra, C., Turatto, M., Pastorello, A., et al. 2011, MNRAS, 417, 261
Inserra, C., Turatto, M., Pastorello, A., et al. 2012, MNRAS, 422, 1122
Itoh, R., Ui, T., & Yamanaka, M. 2012, CBET, 3054, 2
Jerkstrand, A., Fransson, C., Maguire, K., et al. 2012, A&A, 546, A28
Jerkstrand, A., Smartt, S. J., Fraser, M., et al. 2014, MNRAS, 439, 3694
Jordi, K., Grebel, E. K., & Ammon, K. 2006, A&A, 460, 339
Kasen, D., & Woosley, S. E. 2009, ApJ, 703, 2205
Kochanek, C. S., Khan, R., & Dai, X. 2012, ApJ, 759, 20
Lenz, D. D., Newberg, J., Rosner, R., Richards, G. T., & Stoughton, C. 1998, ApJS, 119, 121
Leonard, D. C., Filippenko, A. V., Li, W., et al. 2002, AJ, 124, 2490
Leonard, D. C., Pignata, G., Dessart, L., et al. 2012, ATel, 4033, 1
Li, W., Leaman, J., Chornock, R., et al. 2011, MNRAS, 412, 1441
Liszt, H. 2014, ApJ, 780, 10
Litvinova, I. Y., & Nadezhin, D. K. 1985, SvAL, 11, 145
Maguire, K., Di Carlo, E., Smartt, S. J., et al. 2010, MNRAS, 404, 981
Millard, J., Branch, D., Baron, E., et al. 1999, ApJ, 527, 746
Munari, U., Henden, A., Belligoli, R., et al. 2013, NewA, 20, 30
Munari, U., Vagnozzi, A., & Castellani, F. 2012, CBET, 3054, 3
Munari, U., & Zwitter, T. 1997, A&A, 318, 269
Nugent, P., Sullivan, M., Ellis, R., et al. 2006, ApJ, 645, 841
Olivares, E. F., Hamuy, M., Pignata, G., et al. 2010, ApJ, 715, 833
Parrent, J., Branch, D., Troxel, M. A., et al. 2007, PASP, 119, 135
Pastorello, A., Pumo, M. L., Navasardyan, H., et al. 2012, A&A, 537, A141
Pastorello, A., Valenti, S., Zampieri, L., et al. 2009, MNRAS, 394, 2266
Poznanski, D., Butler, N., Filippenko, A. V., et al. 2009, ApJ, 694, 1067
Poznanski, D., Nugent, P. E., Ofek, E. O., Gal-Yam, A., & Kasliwal, M. M. 2012, ATel, 3996, 1
Poznanski, D., Prochaska, J. X., & Bloom, J. S. 2012, MNRAS, 426, 1465
Pumo, M. L., Turatto, M., Botticella, M. T., et al. 2009, ApJL, 705, L138
Pumo, M. L., & Zampieri, L. 2011, ApJ, 741, 41
Pumo, M. L., Zampieri, L., & Turatto, M. 2010, MSAIS, 14, 123
Rizzi, L., Tully, R. B., Makarov, D., et al. 2007, ApJ, 661, 815
Sandage, A., & Tammann, G. A. 1987, A Revised Shapley-Ames Catalog of Bright Galaxies (2nd ed.; Washington: Carnegie Institution)
Schlafly, E. F., & Finkbeiner, D. P. 2011, ApJ, 737, 103
Schlegel, D. J., Finkbeiner, D. P., & Davis, M. 1998, ApJ, 500, 525
Siviero, A., Tomasella, L., Pastorello, A., et al. 2012, CBET, 3054, 4
Skillman, E. D., & Gallart, C. 2002, in ASP Conf. Proc., Vol. 274, Observed HR Diagrams and Stellar Evolution, ed. T. Lejeune & J. Fernandes (San Francisco, CA: ASP), 535
Skrutskie, M. F., Cutri, R. M., Stiening, R., et al. 2006, AJ, 131, 1163
Smartt, S. J. 2009, ARA&A, 47, 63
Smartt, S. J., Eldridge, J. J., Crockett, R. M., & Maund, J. R. 2009, MNRAS, 395, 1409
Springob, C. M., Haynes, M. P., Giovanelli, R., & Kent, B. R. 2005, ApJS, 160, 149
Stockdale, C. J., Ryder, S. D., Van Dyk, S. D., et al. 2012, ATel, 4012, 1
Tomasella, L., Cappellaro, E., Fraser, M., et al. 2013, MNRAS, 434, 1636
Turatto, M., Benetti, S., & Cappellaro, E. 2003, in Proc. ESG/MPA/MPE Workshop, From Twilight to Highlight: The Physics of Supernovae, ed. W. Hillebrandt & B. Leibundgut (Berlin: Springer), 200
Utrobin, V. P., & Chugai, N. N. 2009, A&A, 506, 829
Utrobin, V. P., & Chugai, N. N. 2011, A&A, 532, A100
Valenti, S., Fraser, M., Benetti, S., et al. 2011, MNRAS, 416, 3138
Van Dyk, S. D., Cenko, S. B., Poznanski, D., et al. 2012, ApJ, 756, 131
Walmswell, J. J., & Eldridge, J. J. 2012, MNRAS, 419, 2054
Weaver, T. A., & Woosley, S. E. 1980, in Ninth Texas Symp. Relativistic Astrophysics (New York: New York Academy of Sciences), 335
Yadav, N., Chakraborti, S., & Ray, A. 2012, ATel, 4010, 1
Zampieri, L., Pastorello, A., Turatto, M., et al. 2003, MNRAS, 338, 711